This is a repository copy of *Outstanding stability and photoelectrochemical catalytic performance of (Fe, Ni) co-doped Co3O4 photoelectrodes for solar hydrogen production*.

Outstanding stability and photoelectrochemical catalytic performance of (Fe, Ni) co-doped Co_3O_4 photoelectrodes for solar hydrogen production

Alhoda Abdelmoneim[1], Ahmed Naji[1], Erik Wagenaars[2], Mohamed Shaban[1,3*]

[1]Department of Physics, Faculty of Science, Beni-Suef University, Beni-Suef, 62514, Egypt

[2]York Plasma Institute, Department of Physics, University of York, York, YO10 5DD, UK.

[3] Department of Physics, Faculty of Science, Islamic University in Almadinah Almonawara, Almadinah Almonawara, 42351, Saudi Arabia.

Abstract

In this work, pure and (Fe, Ni) co-doped Co_3O_4 nanostructured photoelectrodes of different doping levels and thicknesses were manufactured at constant substrate temperature (450^oC) using the spray pyrolysis technique. In addition to the chemical compositions; the structural, optical, electrical, and photoelectrochemical (PEC) properties were investigated through the use of various analysis techniques. By increasing the codpoing ratio to 6%, the low energy band gap is decreased from 1.43 to 1.3 eV and the high energy bandgap is increased from 2.63 to 2.87 eV, in addition to the reduction in particle size from 30.2 to 12.0 nm. The high energy gap vanishes by increasing the codoped film's spread volume to 60 ml. X-ray photoelectron spectroscopy of 6%(Fe, Ni)-60ml Co_3O_4 confirms the existence of $Ni^{2+,3+}$ and $Fe^{2+,3+}$. Among the studied photoelectrodes, the 6%(Fe, Ni)-60ml Co_3O_4 photoelectrode displays a photocatalytic hydrogen output rate of 150 mmol/h.cm^2 @-1V in 0.3M Na_2SO_4 electrolyte. The photocurrent density of 6%(Fe, Ni)-60ml photoelectrode reached up to 13.6 mA/cm^2@-1V with an IPCE (incident photon to current conversion efficiency) of ~42%@405 nm and STH (solar to hydrogen conversion efficiency) of ~11.37%, which are the highest values yet for Co_3O_4-based photocatalysts. The value of ABPE(applied bias photon-to-current efficiency) is 0.34%@(-0.28V and 636nm). Interestingly, this photoelectrode shows a photogenerated current density of -0.14 mAcm^{-2} at 0 V and a PEC current onset over 0.266V. The thermodynamic parameters, corrosion parameters, PEC surface areas, Tafel slopes, and impedance spectroscopies are also being studied to confirm and classify the PEC H_2 production mechanism. The 6%(Fe, Ni)-60ml Co_3O_4 photoelectrode stability/reusability shows only a 6.6% reduction in PEC performance after ten successive runs at -1V with a corrosion rate of 1.2 nm/year. This work offered a new codoping strategy for the design of highly active Co_3O_4 based photocatalyst for the generation of solar light-driven hydrogen.

Keywords: Co_3O_4 thin films; (Fe, Ni)-codoping; Photoelectrocatalytic hydrogen production; Conversion efficiencies, Corrosion parameters, impedance spectroscopy

Corresponding author: E-mails: mssfadel@aucegypt.edu; mohamed.fadel@science.bsu.edu.eg

1. Introduction

Hydrogen is envisioned as a valuable commodity and a promising sustainable fuel. It is used in fuel cells where it combines with oxygen (from the air) to produce water and energy according to the chemical reaction ($H_2+1/2$ O_2 H_2O +Energy)[1]. Steam reforming of hydrocarbons is a popular method for the production of hydrogen; about 90% of the manufactured hydrogen is produced in this way[2]. This process is carried out under high-pressure and high-temperature conditions, up to 650^oC. The process of the steam reforming of hydrocarbons causes the production of greenhouse gases such as carbon monoxide and carbon dioxide, which play a deleterious role in climate change and global warming[3].

Recently, scientists are intensifying their efforts to solve the world's energy problem by finding renewable and environmentally friendly sources of energy. Sunlight and water are the most important renewable and eco-friendly sources. Water accounts for $\sim$ 71 percent of the Earth's surface [4], and visible light represents the largest percentage (~43%) of the regular solar light [5], so it is beneficial to exploit these in the energy production sector. Solar light and water can be used to obtain hydrogen fuel through several methods: photocatalytic [6], photo-biological [7], and photoelectrochemical (PEC) [8]. PEC water splitting is an effective, low cost and sustainable method for hydrogen production using solar energy and water using semiconductor material as a photoactive medium [9]. The U.S. Department of Energy has established some criteria for the economic feasibility of the application of PEC water splitting technology for hydrogen production. These criteria include 10% conversion efficiency, material durability > 2000 h, current density (J_{pc}) of 10-15 mA/cm^2 [10].

Semiconductor materials including various types such as selenides, sulfides, tellurides, nitrides, and metal oxides show photoresponse to the PEC-water splitting process, a behavior attributed to the existence of a suitable energy bandgap for such materials. Metal oxides are characterized by their abundance in nature, chemical stability, low cost, ease of synthesis, charge separation, and collection efficiency in PEC cells [11, 12]. The use of p and n-type semiconductor metal oxides as photocathodes and photoanodes for PEC water splitting such as titanium dioxide (TiO_2), hematite (α-Fe_2O_3), zinc oxide (ZnO) and tungsten trioxide (WO_3) was the focus of studies [13-16].

Cobalt oxide is a common semiconductor metal oxide, with three main phases known to date: cobaltosic oxide (Co_3O_4), cobaltic oxide (Co_2O_3), and cobaltous oxide (CoO) [17]. Co_3O_4 is known to be stable at a temperature below 800^oC [18]. Cobaltosic oxide (Co_3O_4) is most promising for PEC water splitting. It is a p-type semiconductor with a spinel structure and a mixed-valence (Co^{3+}, Co^{2+}) where the Co^{3+} ion occupies octahedral sites and the Co^{2+} ion occupies the lattice tetrahedral sites[19]. It is widely used in many scientific

applications such as biosensors[20], gas sensor [21], lithium-ion batteries[22], supercapacitors[23], photocatalytic dye removal [24]. Deposition methods for Co_3O_4 thin films include sol-gel [25], chemical vapor deposition CVD [26], dip coating[27], pulsed laser[28], spurting technique [29]. Moreover, Co_3O_4 has a dual-bandgap structure, offering separate band states, which is beneficial for thermalization-related losses in the hydrogen generation powered by sunlight [30]. Finally, it is earth-abundant [31], environmentally friendly[32], chemically stable in both acidic and alkaline electrolytes, and has an appropriate energy gap between 1.5 eV and 2.6 eV [33]. Co_3O_4 was reported as an effective oxygen evolution reaction (OER) catalyst for the PEC water splitting process by Zhang et al. [34]. Also, it was reported as a hydrogen evolution reaction catalyst (HER) by Hong et al. [35]. This indicates the dual-function (OER, HER) of Co_3O_4 in the PEC water splitting process.

The performance of cobaltosic oxide in the PEC water splitting process is still limited for several reasons. First, the indirect optical bandgap of Co_3O_4 is theoretically inappropriate for the use of light absorption applications [33]. Second, an additional bias voltage is required to separate the charge carriers[36]. Third, the high recombination rates for the photogenerated electrons and holes is considered as the main obstacle that limits the PEC performance of the Co_3O_4 [35]. By inserting charge traps, the problem of the high recombination rate of the produced charge carriers can be avoided, thus extending the recombination time [37]. Doping of Co_3O_4 can introduce charge traps, with the most common elements used being transition metals such as Fe, Ni, Cr, V, Cu, and Mn. Doping with these elements can lead to an increase in photocatalytic performance. Fe, Mn, and Cu elements are capable of trapping both holes and electrons, whereas Cr and Ni can only trap single-charge carriers [37]. Gasparotto et. al. studied the impact of fluorine doping on the PEC efficiency of Co_3O_4; the number of hydrogen moles obtained for undoped Co_3O_4 was 45 mmol h^{-1} g^{-1} while the number of moles increased to 213 mmol h^{-1} g^{-1} by doping with fluorine [38].

Our work focuses on the properties of pure and (Fe, Ni) co-doped Co_3O_4 thin films. The effect of the codoping level on different properties of Co_3O_4 has been investigated using different techniques, and for the first time, on the performance of (Fe, Ni) co-doped Co_3O_4 photoelectrodes relative to the pure Co_3O_4 in the PEC water splitting process. We choose nickel doping because its atomic radius is approximately the same as that of cobalt. A slight increase in doping concentration is important to adjust the band gaps without altering the crystal structure of the electrode. Whereas Fe-doping was previously used to extend the lifetime of the charge carriers and then lower the rate of recombination of electron-hole for other metal oxides such as ZnO [39]. All our films were deposited using a spray pyrolysis technique. The effects of doping concentration and the amount of sprayed solution on the physical properties and PEC-activity of the deposited films are investigated. Also, the stability and reusability of the optimized photoelectrode are studied. Finally, impedance spectroscopy measurements are performed and the effect of reaction temperature on the PEC performance is evaluated.

2. Experimental

2.1. Materials

Cobalt(II) nitrate (Co $(No_3)_2.6H_2O$, MW=291.03 g/mol), nickel chloride ($NiCl_2.6H_2O$, MW=237.69 g/mol) and sodium sulphate (Na_2SO_4, MW=142.04 g/mol) were purchased from Oxford Lab (India), iron nitrate($Fe(NO_3)_3·9H_2O$, MW= 403.999 g/mol) was purchased from Piochem company (Egypt). The purity of all chemicals was 99% and all chemicals were used as purchased without any purification processes.

All reactions were carried out using double distilled water. Microscope slides with a thickness of 1 - 1.2 mm were used as a glass substrate for deposition of the films

2.2. Co_3O_4 thin film preparation

Pure and (Fe, Ni) co-doped Co_3O_4 thin films were prepared using a spray pyrolysis technique[40, 41]. All films were deposited onto an amorphous glass substrate at constant temperature $450°C$, the substrate to nozzle distance, and the airflow rate were 30 cm and 25 L/min respectively. In all depositions, the molarity of the precursor solution kept constant at 0.1 M.

Two sets of samples were deposited. In the first set, we sprayed a constant amount (10ml) of the cobalt(II) nitrate with different amounts of the dopants. Equal amounts of iron nitrate and nickel chloride, i.e. 2, 4, and 6 weight %, were added to the cobalt(II) nitrate solution. We refer to this set as a set 1, containing the samples; pure, 2%(Fe, Ni)-10mL, 4%(Fe, Ni)-10mL, and 6%(Fe, Ni)-10mL. The second set was deposited by spraying different amounts (10, 20, 60) ml of the cobalt(II) nitrate solution which contains 6 wt.% of the dopants. The other parameters of the deposition were kept the same. This set is referred to as set 2, containing 6% (Fe, Ni)-10mL, 6% (Fe, Ni)-20mL, and 6% (Fe, Ni)-60mL samples.

2.3. Samples Characterization

A Bruker / Siemens D5000 diffractometer (λ=1.54Å) was used for obtaining the X-ray diffraction (XRD) pattern of the deposited films. The optical behavior of the films in spectral range 400-1100 nm was examined using a PG Instruments T70 spectrophotometer. The chemical composition was analyzed using Energy Dispersive X-ray spectroscopy (EDS, JEOL JED-2300 SEM). X-ray photoelectron spectroscopy (XPS), AXIS-NOVA, Kratos analytical Ltd, UK was used for investigating the oxidation states of the elements.

2.4. PEC water splitting measurements

The photoelectrochemical (PEC) behavior using a Keithly measurement-source unit (Tektronix Company, model: 2400) and LabTracer software under the illumination with a 400 W metal-halide Lamp (Newport, 66926-500HX-R07) in combination with a set of linear optical filters in 0.3 M (100 ml) Na_2SO_4 at 30 ºC (room temperature). The voltage sweep rate was 1 mV/s. The pure and codoped Co_3O_4 electrodes have a 1cm^2 surface area. The PEC current density (J_{ph}) versus voltage was measured in dark, monochromatic, and white light illumination. Also, the sample stability was studied through the measurement of current density (J_{ph}) as a

function of time. The effect of temperature of the Na2SO4 solution on J_{ph}-Voltage behaviors was measured under white light illumination for temperatures in the range 45 – 65 °C.

3.Results and discussion

3.1. X-ray diffraction and microstructural study

Fig. 1a, shows all XRD patterns of pure and (Fe, Ni) co-doped cobalt oxide films at room temperature 25^0C, a wavelength of 1.54 Å, a scan rate 0.02 degree. s^{-1} and a 2-theta range of 10-80°. As can be seen, the main diffraction peak for all films is around a 2-theta value of 36.8°. This peak corresponds to the (311) diffraction plane of the Co_3O_4 face-centered phase (ICDD number 76-1802). No other peaks belonging to other phases were observed, confirming the singularity of the Co_3O_4 phase and the successful doping of these films. The (311) plane has been reported as the main diffraction peak of the Co_3O_4 phase by many authors using different techniques of preparation[27, 42]. In all films the intensities of the recorded peaks are noticed to be week. Such small intensities of the diffraction peaks has been recorded before in our previous work [19, 40]. The small peaks intensities could be attributed to the high cooling rate the films subjected to since all films are taken directly from the hot surface (450° C) which gives a high rate of cooling since the film goes to room temperature in less than a minute.

The observation that the (311) plane is the main peak for all pure and (Fe, Ni) co-doped samples could be attributed to the high structure factor value of (311) plane in the Co_3O_4 structure.

Using the VESTA program, the structure factor value was obtained for pure Co_3O_4 using the 36.899 CIF file. Doping can be done by replacing cobalt ions with Ni and Fe in the program. For all samples, pure and doped, the (311) plane is calculated to have the highest structure factor plane with a relative intensity of 100%. The observed reduction in the main peak intensity upon doping could be attributed to the increase in strain values because of the difference between the atomic radii between the Co ions and the dopants. A small shift of the main peak towards lower 2-theta value is observed upon doping for all films except sample 6%(Fe, Ni)-10 ml in which the main peak shifted to higher 2-theta value, all values of the mean peak shift($\Delta 2\theta$) recorded in Table 1.
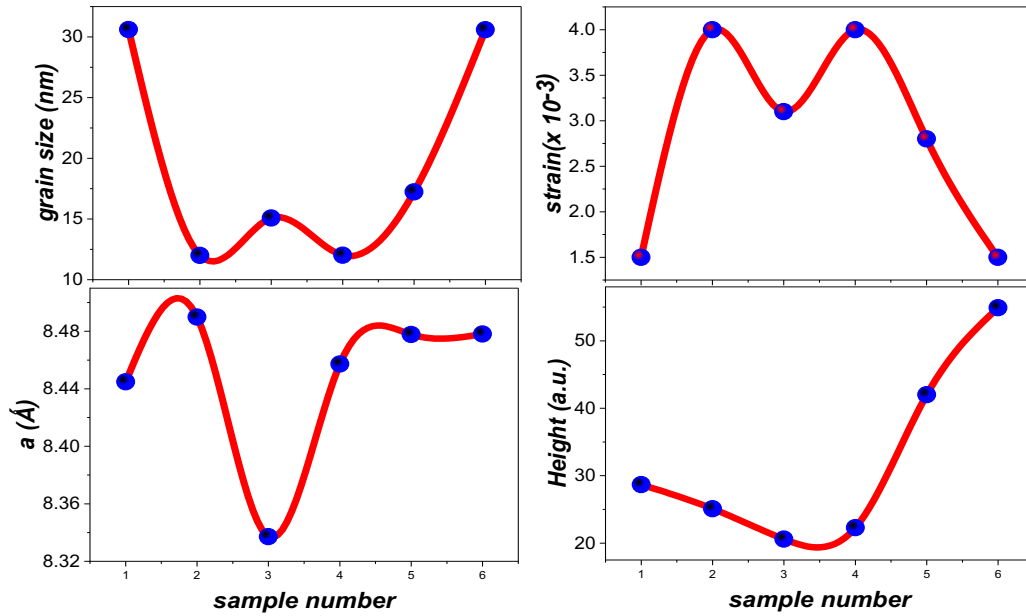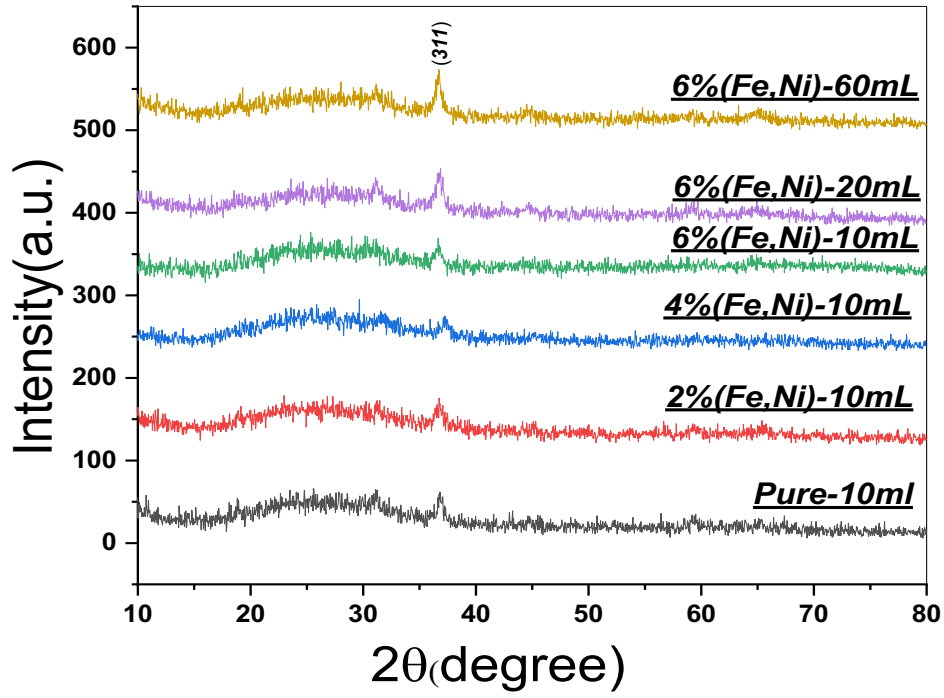
Fig.1. (a)XRD diffraction patterns, (b) grain size, (c) lattice constant, (d) strain, and (e) height of (311) plane for pure and (Fe, Ni) co-doped films. Sample code: (1) pure, (2) 2%(Fe, Ni)-10mL, (3) 4%(Fe, Ni)-10mL, (4) 6%(Fe, Ni)-10mL, (5) 6%(Fe, Ni)-20mL, and (6) 6%(Fe, Ni)-60mL.

The full width at half maximum (FWHM) of the (311) XRD peak has been used to determine the grain size of the films using the Scherer's method, described in equation (1)[43]:

$$D = \frac{k\lambda}{\beta \cos \theta} \quad (nm) \qquad (1)$$

where D represents grain size, k is the shape factor (0.9), λ is the wavelength of X-ray (0.154 nm), β is the FWHM estimated from XRD patterns, θ is the Bragg angle measured in radian. The average grain size of pure Co_3O_4 film was found to be ~30.6 nm. Upon doping the grain size values show a significant variation. The grain size for all films in set 1 shows lower values than the pure film. Films deposited by spraying (20, 60) ml of the precursor solution show an increase in the grain size due to the increase in the film thickness and the deposition time. All recorded grain size values are presented in Fig. 1b and Table 1, whereas the sample number 1, 2, 3, 4, 5, and 6 refers to pure, 2%(Fe,Ni)-10ml, 4%(Fe,Ni)-10ml, 6%(Fe,Ni)-10ml, 6%(Fe,Ni)-20ml, 6%(Fe,Ni)-60ml films, respectively.

Such variation in the grain size of samples in set 1 could be explained in the frame of the pinning effect [41, 44]. The (Fe, Ni) incorporated into the Co_3O_4 matrix will be acting as an impurity and might become an obstacle that limits the growth of the grains, causing a reduction in the grain size. The relation between the grain size and the radius of pining particles (R) in addition to the volume fraction f_v of these particles can be described by equations 2-4 [41]:

$$D = \frac{4\alpha R}{3 f_v} \qquad (2)$$

where α is defined as a geometrical constant.

$$Z = \frac{3 f_v \gamma}{2R} \qquad (3)$$

Z is the Zener drag pinning force, γ the energy of the grain boundary.

$$\therefore \quad D = \frac{2\alpha\gamma}{Z} \qquad (4)$$

From the above equations, increasing the volume fraction of the obstacle (f_v) will lead to higher pining force (Z) and therefore limits the growth of the grains.

The dislocation density (length of dislocation per unit volume) and the strain were estimated using equations 5 and 6 [45]:

$$\delta = \frac{1}{D^2} \qquad (5)$$

$$\varepsilon = \frac{\lambda}{D \sin\theta} - \frac{\beta}{\tan\theta} \qquad (6)$$

where δ is the dislocation density, ε is the strain-induced inside the thin films.

The lattice constant, a, was estimated using equation 7[46]:

$$d_{hkl} = \frac{a}{\sqrt{h^2 + K^2 + L^2}} \qquad (7)$$

Figure 1c displays the lattice constant for all deposited films. This variation in the lattice constant values with changing upon doping could be attributed to the random selection of the dopant atom to the lattice sites. Co3O4 unit cell is a complicated cell with 32 atoms per cell. The sites where the dopant will be placed are randomly selected during the deposition especially with the competition of the Ni and Fe ions to substitute the Co ions. This may result in such an inconsistent variation in the lattice parameters values.

The theoretical density σ_x is calculated from the value of the lattice parameter, using equation 8[47]:

$$\sigma_x = \frac{A*n}{V*N_A} \qquad (8)$$

where σ_x is the theoretical density of Co3O4, A is the atomic weight, N_A is the Avogadro's number, n is the number of molecules per unit cell, V is the volume of the unit cell. All calculated values of σ_x have been recorded in table1. It is found that σ_x of pure Co3O4 films equals to 5.31 g/cm³. The literature value of the density of Co3O4 is 6.11 gm/cm³ [48]. This difference in density could be attributed to the nature of sample preparation and deposition parameters. It is worth noting here that the deposition condition changes the lattice volume which is an important parameter in density determination.

The thickness of all deposited films estimated via the weight difference method using equation 9 [48]:

$$t = \frac{m}{A \rho} \qquad (9)$$

where t represents the thickness, m is the mass of the deposited film over the substrate, A represents the area of the film, ρ the density of the deposited film. It is found that all doped films have a larger thickness than the pure film which has a thickness of 140 nm. This increase in the thickness of doped films with respect to pure film can be explained through the film composition. It is known that the Co-O bond length is about 2.13 Å[49] which is larger than the 1.73 Å of the Fe-O
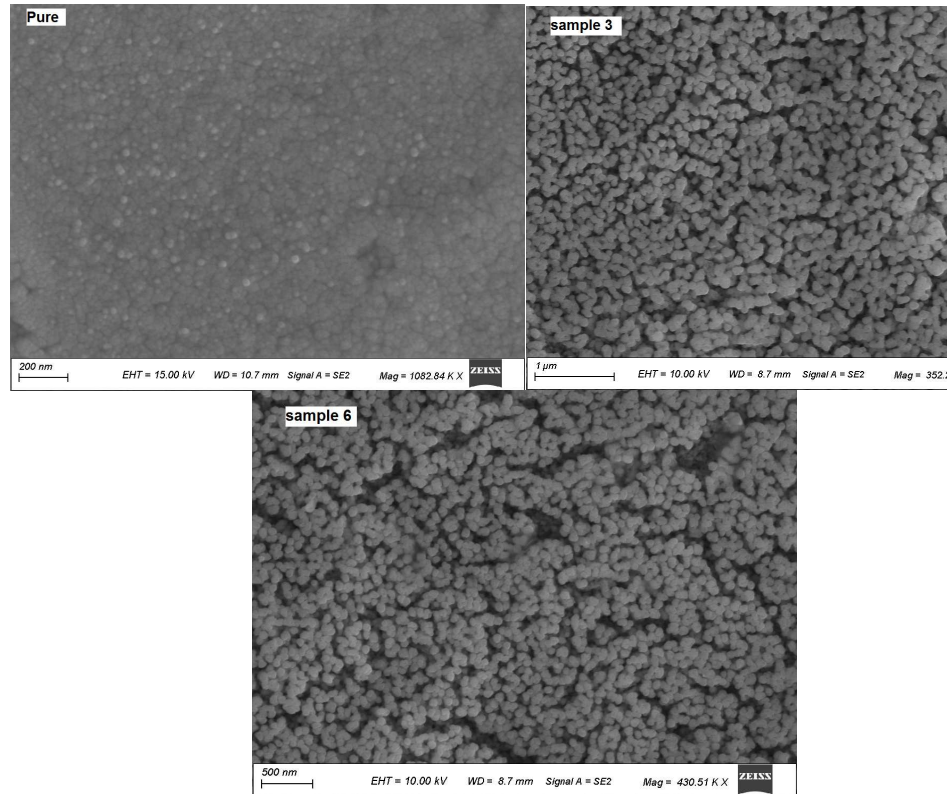

Figure 2:- SEM images for samples 1, 3 and 6.

bond [50] and 2.08 Å for the Ni-O bond [51]. Such larger bond length makes the escape of oxygen from the deposited film at high temperatures harder than from pure cobalt oxide film. This means the dopants bring more materials in the deposited film, which consequently increases the thickness.

Figure 2 shows the SEM photos for samples pure1, 3, and 6. The grain size obtained for the selected films was found to be 30.6, 91.57, and 91.22 nm. The grain size values were estimated by using ImageJ software[52]. The grain size values from the SEM images are higher than those values obtained from Scherer's method. That could be attributed to the difference in the measurement technique and the possible agglomeration in the film during deposition. In our previous work on Co3O4 [40] agglomeration phenomena were observed and discussed.

Table 1: XRD parameters for all deposited films.

Sets	Set 1				Set 2	
Sample number	1	2	3	4	5	6
Sample name	Pure-10 mL	2%(Fe,Ni)-10 mL	4%(Fe,Ni)-10 mL	6%(Fe,Ni)-10 mL	6%(Fe, Ni)-20 mL	6%(Fe, Ni)-60 mL
G.S (nm)	30.6	12	15.08	12.02	17.23	30.59
2θ(degree)	36.86	36.66	37.36	36.81	36.72	36.719
a (Å)	8.44	8.48	8.33	8.45	8.47	8.47
V (Å)	602.25	611.94	579.5	604.9	609.32	609.39
d-spacing(Å)	2.43	2.45	2.4	2.44	2.44	2.44
$\Delta 2\Theta$ (degree)	0.04	0.24	-0.46	0.08	0.18	0.18
Height(cts)	28.67	25.1	20.59	22.28	42.02	54.91
β (radian) $*10^{-3}$	4.77	12.16	9.69	12.15	8.47	4.77
strain $*10^{-3}$	1.5	4.0	3.1	4.0	2.8	1.5
δ(lines/nm^2)$*10^{-3}$	1.1	6.9	4.3	6.9	3.3	1.1
σ_x (gm/cm^3)	5.31	5.23	5.51	5.28	5.24	5.24
Thickness (nm)	140.98	206.98	672.02	771.57	634.86	2157.74

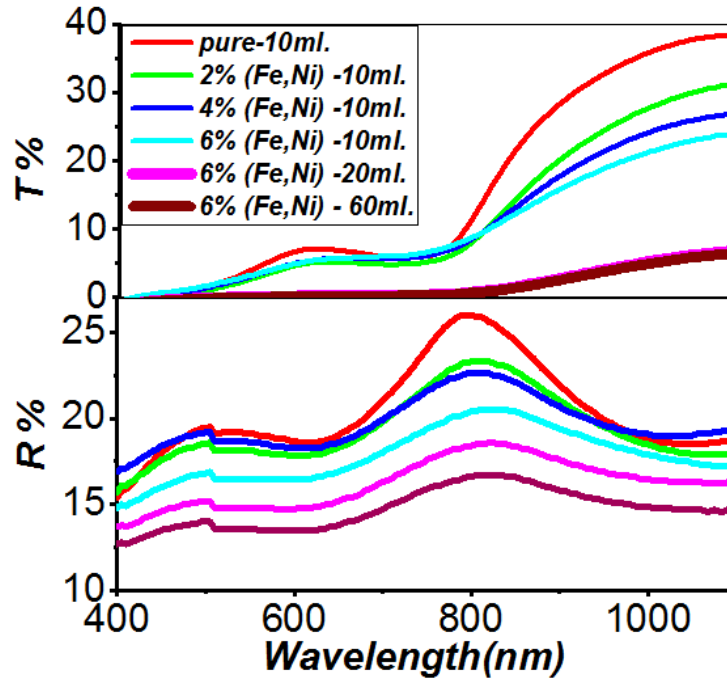Fig. 3. Optical transmission % and reflection% for all deposited samples

3.2. Optical characterization

The transmission and reflection spectra of all films have been recorded and presented in Fig. 3. As observed three regions in the transmission spectra can be recognized, a low transmission region in the wavelengths below 500 nm, a medium transmission region between 500 to 780 nm and a high transmission region above 800 nm.

In the reflection spectra, a reflection peak was found around 820 nm in all films. Also, the transmission and reflection values decreased gradually with increased doping concentrations.
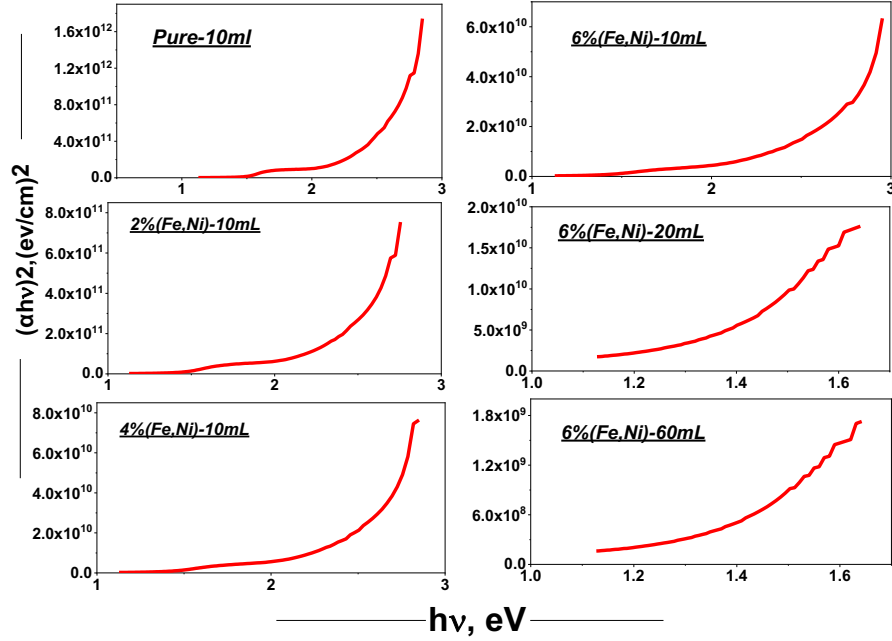

Fig. 4. Variation of $(\alpha h\nu)^2$ versus $h\nu$ for all deposited films to calculate the bandgap.

The direct allowed band gap of all films was estimated using Tauc's equation [47]:

$$(\alpha\upsilon)^2 = B(h\upsilon - E_g) \qquad (10)$$

where B is a constant), h is Planck's constant, ν is the photon frequency, E_g is the optical band gap and α is the absorption coefficient. The absorption coefficient can be deduced from[53]:

$$\alpha = \frac{1}{d}\ln\left(\frac{(1-R)^2}{T}\right) \qquad (11)$$

where d represents the thickness of the film. All band gaps of all deposited films were estimated by extrapolating a straight line from the $(\alpha h\nu)^2$ and $(h\nu)$ plot as in Fig. 4. The intersection point with the $h\nu$ axis represents the band gap value. All values of band gaps are listed in table 2. All films were found to have two direct optical band gaps except 6% (Fe, Ni)-20 ml and 6%(Fe, Ni)-60 ml doped films which appeared to have a single direct optical band gap (Eg_1). In Co_3O_4 thin films, the valence band (VB) is formed due to the contribution of O^{2-} states, while Co^{2+} gives the main contribution to the conduction band (CB). The existence of Co^{3+} centers in Co_3O_4 creates a sub-band within the energy gap. Consequently, there are two optical band gaps, Eg_1 and Eg_2, where Eg_1 is assigned to $O^{2-} \rightarrow Co^{3+}$ charge transfer whilst Eg_2 is assigned to $O^{2-} \rightarrow Co^{2+}$ charge transfer. Eg_2 is considered as the true energy gap that corresponds to inter-band transitions (VB to CB

excitation) [54]. As presented in table 2, the values of Eg_1 decrease for increasing doping ratio while the value of Eg_2 increases with doping.

The refractive index of all deposited films was estimated using equation 12 [55]:

$$n = \frac{1+R}{1-R} + \sqrt{\frac{4R}{(1-R)^2} - k^2}$$ (12)

where R is the reflectance and k is the extinction coefficient of the films. The values for k were estimated via the relation $= \frac{\lambda\alpha}{4\pi}$. As shown in Fig. S1(a) (supplementary data), the refractive index, n, increases with an increasing wavelength between 550 and 825 nm for all films. Above ~825nm, the refractive index decreases with wavelength as in a normal dispersion relation.

For most semiconducting materials, Wemple Di-Domenico suggested a single oscillator model describing a relation between the refractive index and the oscillator strength below the optical bandgap. This is described in equation 13 [55]:

$$n^2 - 1 = \frac{E_d E_o}{E_o^2 + (hv)^2}$$ (13)

where E_d and E_o represents the oscillator strength and oscillator energy respectively, E_d is a measure of interband optical transition strength but E_0 indicates the average electronic transition excitation energy. The values of E_d, E_0 are determined from the plot of $(n^2-1)^{-1}$ versus $(hv)^2$ as represented in Fig. S1(b), whereas the slope and the intercept of the linear portion of this relation are $(E_d E_0)^{-1}$ and (E_0 / E_d) respectively. The derived values of E_d and E_0 are presented in table 2. M_{-1}, M_{-3} moments of spectra also calculated using the values of E_d, E_0 according to $M_{-1} = E_d/E_0$, $M_{-3} = E_d/E_0^2$, all values of M_{-1}, M_{-3} moments listed in table 2.

The zero-frequency refractive index (n_0), also known as the deposited film's static refractive index, was estimated using [56]:

$$n_o = \sqrt{\left(1 + \frac{E_d}{E_0}\right)}$$ (14)

The estimated values of n_0 are presented in table 2 and it is in good agree with the values obtained by C. Ravi Dhas et al. [56].

Table 2: Band gap values (Eg_1, Eg_2) in eV, oscillator energy (E_0), oscillator strength (Ed), moments of the spectra(M_{-1}, M_{-3}), static refractive index (n_0), activation energy values (E_{a1}, E_{a2}) in eV.

sample	Eg_1	Eg_2	E_0	E_d	M_{-1}	M_{-3}	n_0	E_{a1}	E_{a2}
Pure-10ml	1.48	2.63	1.87	5.5	2.94	1.56	1.98	0.11	-
2%(Fe,Ni) -10ml	1.42	2.65	2.07	6.9	3.33	1.61	2.08	0.075	-
4% (Fe,Ni)-10ml	1.39	2.77	2.23	8.6	3.85	1.72	2.2	0.072	-
6%(Fe,Ni)-10ml	1.36	2.87	2.34	8.69	3.71	1.57	2.17	0.053	0.15

6%(Fe,Ni)-20mL	1.3	-	2.75	9.82	2.57	1.29	2.13	0.07	-
6% (Fe, Ni)-60 ml	1.3	-	2.70	9.01	3.33	1.23	2.08	0.065	-

3.3. Chemical composition

The chemical composition of the pure and (Fe, Ni) co-doped films was investigated using Energy Dispersive X-ray spectrometer (EDX). Fig. 5a and Fig. 4b shows the EDX spectra of pure and 6%(Fe, Ni) - 60 ml co-doped films respectively. The EDX spectrum of pure films Fig. 4a indicates the presence of O and Co peaks which appeared at 0.52 keV and 6.92 keV respectively. The sharp peaks at 1.73 keV and 3.69 keV reveal the presence of Si and Ca, respectively.

The EDX spectrum of 6%(Fe, Ni)-60 ml co-doped films, Fig. 5b indicates the presence of for Fe and Ni peaks at 6.39 keV and 7.47 keV respectively, this confirms the incorporation of (Fe, Ni) into the Co_3O_4 matrix and provides evidence of successful doping. The atomic percentage (at%) of O, Co, Ni, and Fe elements in all deposited films are listed in Table S1(supplementary data). For the films deposited by spraying 10 ml of the precursor, we measure close to 80% O which is far too high if it was from the film only because the stoichiometric would mean 43% Co and 57% O. This suggest part of O is from the glass substrate. The O signal decreases to ~53.6% by increasing the sprayed volume to 60 mL. Other elements like Si and Ca are presented as a result of substrate contribution. Both Fe and Ni atomic percentage increase with increasing doping level and sprayed volume. The atomic percentage values for Ni are higher than for Fe, indicating that Ni atoms occupy more sites in the host lattice of Co_3O_4 than Fe atoms. This could be because of the comparable ionic radii of Ni and Co. Consequently, this will affect the structural and the optical properties of the deposited films.
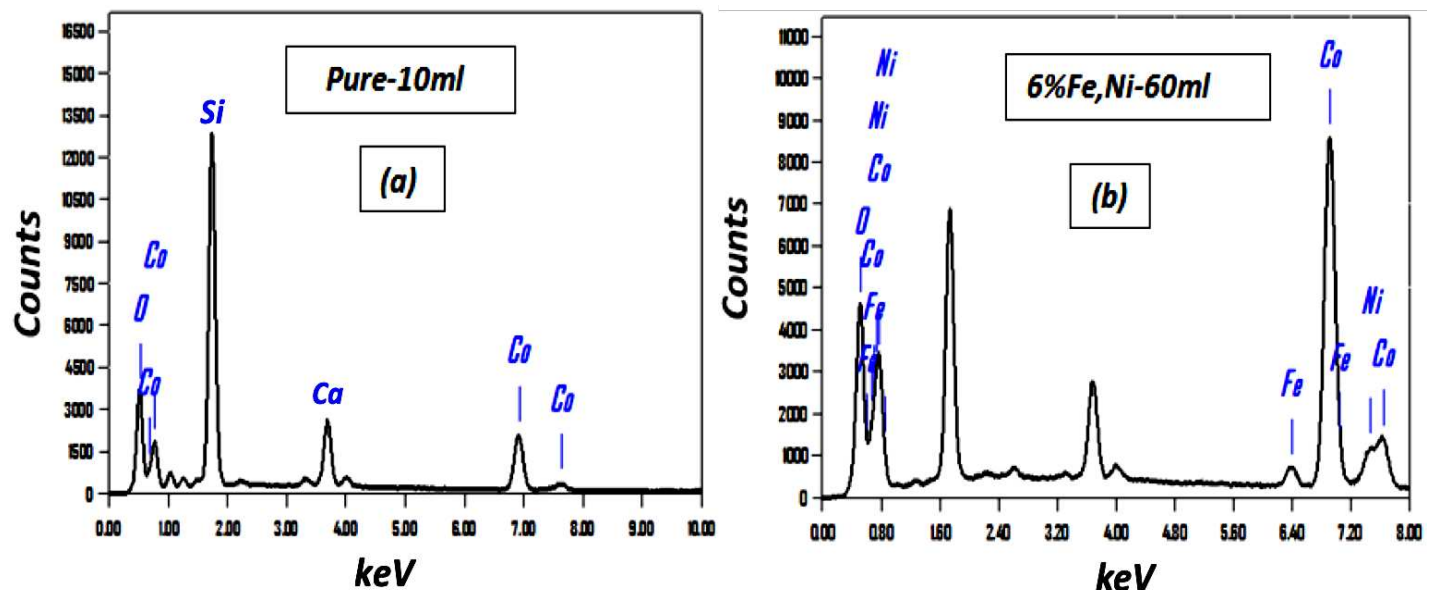
3.4. X-ray photoelectron spectroscopy (XPS)

Figure 6 shows the XPS survey spectra of pure Co_3O_4 films. As shown in the figure peaks belong to carbon, oxygen and cobalt were recorded. The positions of these peaks are 285.25, 530.5 and 780.5 eV for carbon, oxygen and cobalt, respectively. The rations of these elements are 50.52, 36.67 and 12.81 % for carbon, oxygen and Cobalt, respectively.

XPS measurements were employed for 6%(Fe, Ni)-60ml co-doped film to demonstrate the oxidation states and the chemical composition of the film. Figure 7a represents the XPS survey scan of the deposited film and the de-convoluted spectra of different elements. Signals at 855.05, 780.24,710.5 and 530.31eV belong to Ni2p, Co2p, Fe2p, and O1s energy levels respectively. In pure film, he Co2p and O 1s peak was recorded at 780.5 and 530.5 eV, respectively. This shift in the positions of the Co2p and O1s peaks is related to the change in the chemical environment because of doping. The small peak centered at 284.98 eV represents the presence of

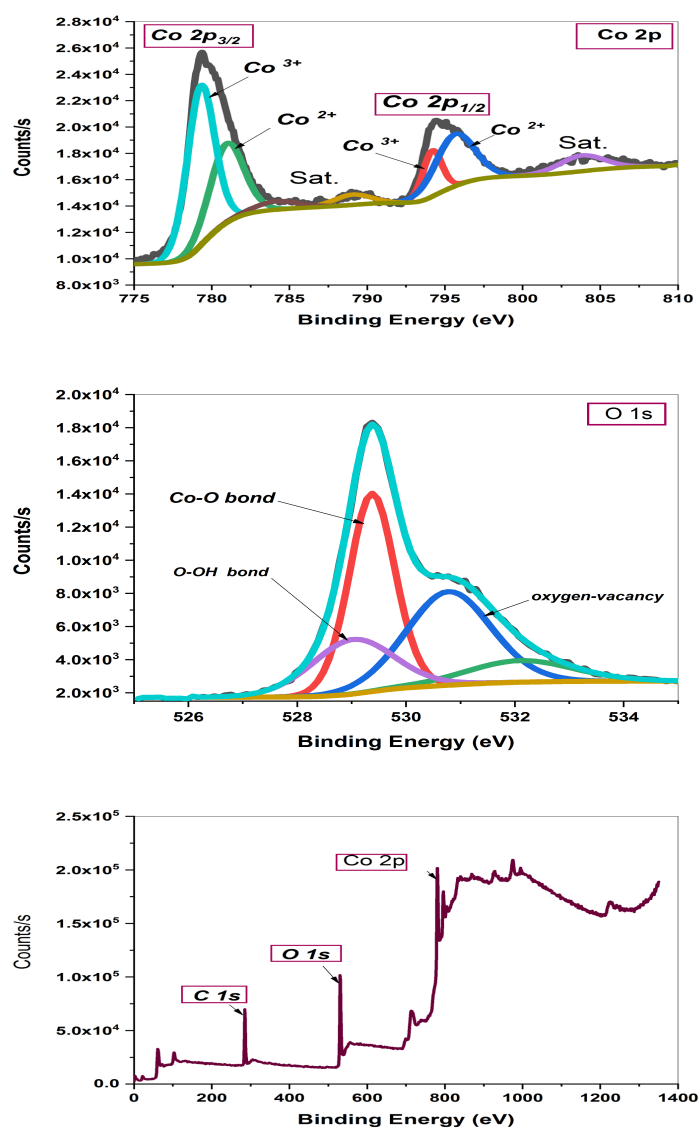Figure 6:- XPS spectra of pure Co3O4 film.

34.75% of carbon. The presence of carbon is expected as a result of carbon accumulation on the surface upon air exposure [57, 58]. Table S2 (supplementary data) lists the atomic percentages of all recorded elements in the deposited film with their valence and atomic radii. Fig. 7b represents the de-convoluted spectrum of Co2p, it includes four peaks at 779.51, 781.16, 794.5 and 796 eV which corresponds to (Co^{3+} $2P_{3/2}$), (Co^{2+} $2P_{3/2}$), (Co^{3+} $2P_{1/2}$) and (Co^{2+} $2P_{1/2}$) respectively. Two other peaks appeared at 788.91 and 803.92 eV which correspond to Co $2p_{3/2}$ and Co $2p_{1/2}$ satellites, respectively. Those peaks positions are slightly different that that recorded in the pure Co3O4 film as shown in figure 6. As shown in the de-convoluted spectrum of Co2p for the pure film, it includes four peaks at 779.36, 781.05, 794.18 and 795.81 eV which corresponds to (Co^{3+} $2P_{3/2}$), (Co^{2+} $2P_{3/2}$), (Co^{3+} $2P_{1/2}$) and (Co^{2+} $2P_{1/2}$) respectively. Also, the satellites peaks are shifted from the peaks recorded in the pure film were the positions are 784.5 and 789.11 eV.

The difference between Co $2p_{3/2}$ and Co $2P_{1/2}$ was found to be 15 eV which is consistent with previous studies[59-61]. Co_3O_4 is a material with mixed-valence cobalt atoms, Co^{2+}(33%) and Co^{3+}(66%)[62]. This makes the Co^{2+}/Co^{3+} ratio for the stoichiometric Co_3O_4 phase is 0.5. The Co^{2+}/Co^{3+} ratio is ~ 0.98 which is very high compared to pure Co_3O_4. These ratios had been calculated with respect to the cobalt content only. Factors like the deposition technique, doping processes, and annealing temperature were found to have a significant effect on the Co^{2+}/Co^{3+} ratio in Co_3O_4 thin films. Z. Wang et al [59] recorded the XPS spectra of different Co_3O_4 nanostructures where the highest Co^{2+}/Co^{3+} ratio was 40.3/59.7 (= 0.675) for nanobelts. In the same work, this ratio reduced to near the normal ratio for nanosheets and nanoplates. The work of H. Wu et al [63] studied the effect of calcination temperature on the Co^{2+}/Co^{3+} ratio. They found that the uncalcinated sample has a ratio of 0.59 which is very close to the pure Co_3O_4 phase. By calcination at a temperature of 450°C the ratio increases to 1.79 and then reduced to 1.2 by increasing the calcination temperature to 650°C.

The high-resolution spectrum of the Ni2p core level is displayed in Fig. 7d. It reveals the presence of both Ni2p$_{3/2}$ and Ni2p$_{1/2}$ and their satellite peaks. The two peaks at 854.7 and 857.7 can be assigned to Ni^{2+}2p$_{3/2}$, Ni^{3+}2p$_{3/2}$ respectively, with their satellite peaks at 860.8, 862.96 eV respectively. The peaks at 870.88 and 872.85 eV are assigned to Ni^{2+}2p$_{1/2}$ and Ni^{3+}2p$_{1/2}$, respectively. The satellite peak at 879.53eV confirms the presence of Ni^{2+}[64-66]. The de-convoluted spectrum of Fe2p is presented in Fig. 7f. It reveals the presence of two peaks at 709.08 and 711.95 eV, confirming the presence of Fe^{2+}2P$_{3/2}$ and Fe^{3+}2P$_{3/2}$ respectively. Their satellite peaks can be seen at 715.28 and 718.59 eV respectively. The peak at 722.8 eV corresponds to (Fe^{2+} 2P$_{1/2}$)[67-69]. The contribution of oxygen in the XPS spectrum can be understood by the de-convoluted O1S peak, shown in Fig. 7c. This peak can be de-convoluted to three peaks centered at 529.43, 531.07, and 531.92 eV. These bands are assigned to Co-O bond (O_L), hydroxyl (O-OH), and oxygen vacancies [70]. Another peak at 533 eV which related to the chemisorbed oxygen is not recorded here[70].
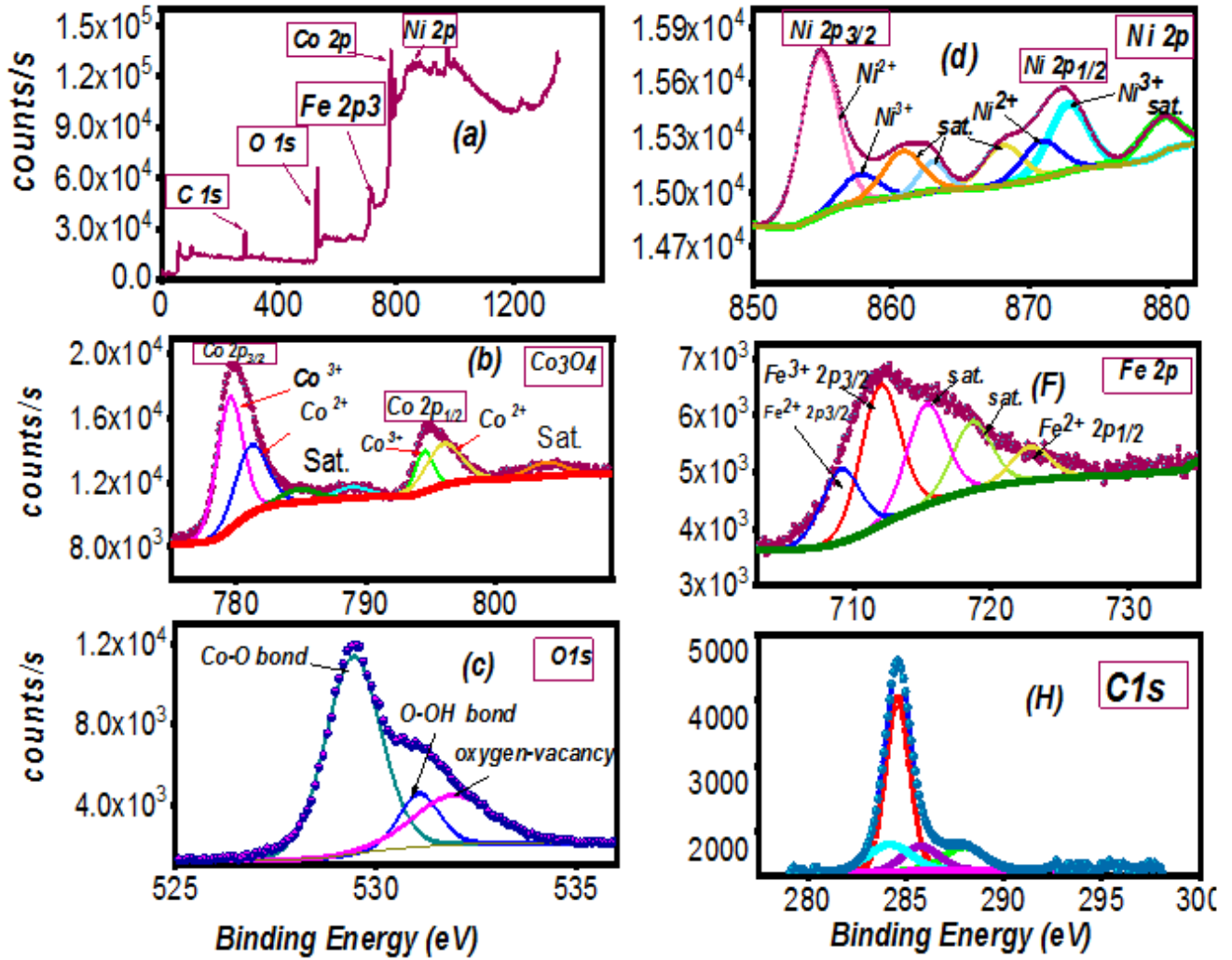
Fig. 7. (a) XPS survey of 6%(Fe,Ni) -60 ml co-doped films; de-convoluted spectra of (b) Co2p,(c) O1s, (d) Ni2p,(f) Fe2p, and (H)C1s .

3.5. Dc conductivity analysis

DC electrical conductivity, σ, of all films was measured by recording resistance against temperature in the range 333 to 483°C. Silver conductive paste was used as a conductive contact, limiting the temperature to 483 °C. Fig. 6 shows the variation of Ln(σ) with 1000/T for all films. As observed all films show an increase in conductivity upon temperature increase, which is typical semiconducting behavior. Also, the pure Co_3O_4 films have the lowest conductivity among all films, i.e. the conductivity increases upon doping. This behavior follows the Arrhenius equation (15):

$$\sigma = \sigma_o e^{\frac{-E_a}{KT}} \qquad (15)$$

where E_a is the activation energy, K is Boltzman's constant, and T is the absolute temperature.

All films show a single straight line in the whole temperature range except for the 6%(Fe, Ni)-10ml film which shows two straight lines. The activation energy of all films is calculated from the slope of the lines and listed in table 2. For the pure Co_3O_4 film, the estimated activation energy was found to be 0.11eV. Aboud et.al[19] studied the DC conductivity of pure Co_3O_4 thin films deposited by spray pyrolysis. They found that the activation energy is 0.189 eV. In a study by Shinde et. al. [71], the activation energy of 0.21eV was found. For all doped films, the conductivity increases with decreasing the activation energy values. In table 2, all values of the activation energy are listed. Such an increase in the conductivity in doped films could be attributed to the increase of the carrier concentration and the film thickness upon doping. Using a thermoelectric probe, the type of charge carrier was checked for all deposited films. All films showed p-type behavior, no change in the type of charge carrier was observed. The reduction of the activation energy with increasing doping with Ni and Fe can be understood from the relation [72]:

$$E_a = E_I - \alpha N_A^{1/3} \qquad (16)$$

where E_I is the ionization energy for an isolated impurity center and α is a constant, N_A is the concentration of the dopant ions. J. A. K. Tareen et al. [73] studied the electrical properties of Ni-doped Co_3O_4 single crystals. They found that the activation energy decreased as the Ni-concentration increased. For pure single crystals, the activation energy was found to be 0.79 eV. However, upon doping with Ni the activation energy decreased to 0.52 eV and to the minimum of 0.4 eV at the highest Ni content. In the same work, all crystals showed p-type conductivity above room temperature, which is in line with the p-type conductivity recorded in this work. M. Manickam et al. [74] studied the electrical conductivity of Fe-doped Co_3O_4. They found that the electrical conductivity increases with increasing Fe content. Two activation energies have been recorded in low and high temperatures. However, the activation energy shows a nonsystematic variation with Fe content.
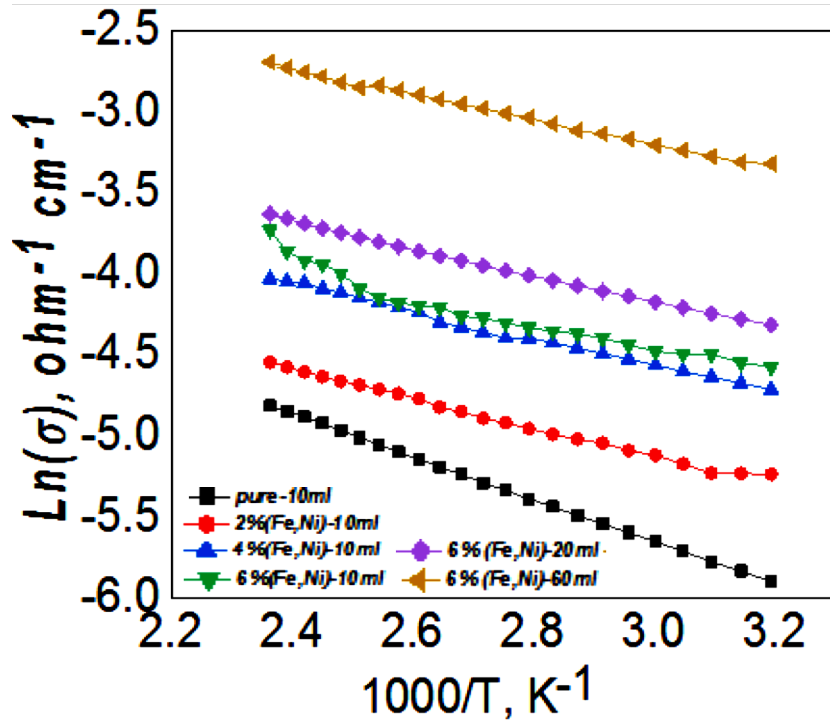
Fig. 6. Variation of Ln(σ) with 1000/T for all films.

3.6. Photoelectrochemical (PEC) measurements

3.6.1. PEC behaviors and stability

PEC characteristics of pure and (Fe, Ni) codoped Co_3O_4 photoelectrodes were measured under standard light illumination of 100 $mW.cm^{-2}$ utilizing a 2400-Keithley measurement-source unit. The photoelectrodes, with surface areas of 1 cm^2, act as the working electrode, while a Pt electrode was used as the counter electrode. Both the working electrode and the counter electrode were immersed in 0.3M sodium sulphate solution (Na_2SO_4), which acts as the redox electrolyte for the PEC water splitting process. The variation of the current density (J_{ph}) under the illumination of white light versus the applied voltage in the range -1V to 1V is presented in Fig. 7a. Using all the working photoelectrodes and under the white light illumination, the J_{ph} is highly increased versus the negative applied potential and almost remains constant versus the positive applied potential. This implies that our electrodes are affected by the white light and are working as photocathodes. For all electrodes, by increasing the negative applied voltage the PEC current density increased as can be expected from an enhancement of the tunneling behavior of the photogenerated carriers. As shown in Fig. 7a, J_{ph} increased with increasing doping level. This may be due to the extending of the optical band gap upon doping into the visible light region, which expedites the rate of the redox reaction and hence facilities the PEC process.

The maximum current density obtained from 6%(Fe, Ni)-60 ml was 13.6 mA/cm^2. This suggests a ~40 fold improvement of the current density compared with the pure Co$_3$O$_4$ photoelectrode (-0.34 mA/cm^2@-1V). It is consistent with the rise in surface charges, the optical expansion of E_{gI} and E_{gII}, and the robust absorption of Vis/IR due to the introduction of (Fe, Ni) codoping. The weak PEC current density of the Co$_3$O$_4$ photoelectrode can be attributed to a reduced density of electron-hole pairs due to recombination processes. Note that 6%(Fe, Ni)10mL and 6%(Fe, Ni)60mL photoelectrodes show light-harvesting with a PEC current density of ~ -0.16 and -0.14 mA cm^{-2} at 0 V, and PEC current onsets over 0.427 and 0.266 V, respectively. It indicates a drop in the interfacial transport resistance after introducing the proper (Fe, Ni) codoping level and highlighted the role of co-dopants in enhancing the PEC efficiencies.
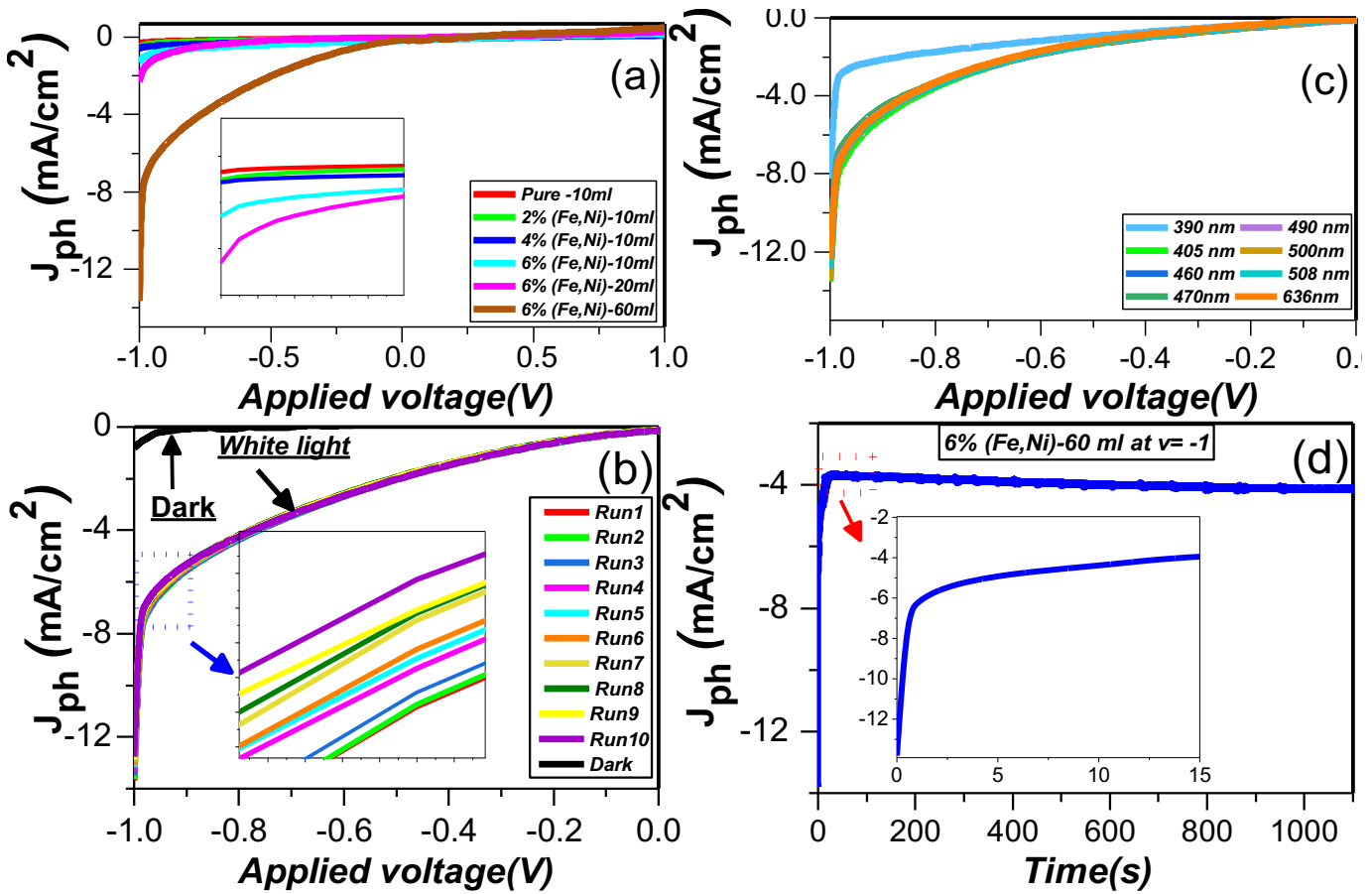

Fig. 7. Variation of J$_{ph}$ versus the applied voltage for (a) all photoelectrodes under white light illumination, (b) 6%(Fe, Ni)-60ml Co3O4 photoelectrode for a different number of runs under dark and white light illumination conditions, and (c) 6%(Fe, Ni)-60ml Co3O4 photoelectrode under monochromatic illumination; and (d) J$_{ph}$ versus exposure time for 6%(Fe, Ni)-60ml Co3O4 photoelectrode at -1V.

The J$_{ph}$ - V curve for 6%(Fe, Ni)- 60 ml electrode was performed under dark conditions and white light illumination for several runs to study the reproducibility of the electrode performance. These results are shown in Fig. 7b. The detected dark current density for 6%(Fe, Ni)-60mL photoelectrode was very small (0.9 mA/cm^2) at -1 V compared to the white light current density (13.6 mA/cm^2), providing evidence for the efficient PEC

water splitting process. Subsequent repeat measurements resulted in a decrease of the photocurrent density from 13.6 mA/cm^2 to 12.7 mA/cm^2 after ten successive runs at -1 V, a decrease of 6.6%. Fig. 7c indicates the variation of J_{ph} versus the applied voltage for 6%(Fe, Ni)-60 ml photoelectrode under monochromatic light illumination using several optical bandpass filters in the visible region with wavelengths from 390 nm to 636±10 nm. The highest current is obtained at 405 nm with J_{ph} = 13.5 mA/cm^2. The least current was obtained at 390 nm with J_{ph} = 8.26 mA/cm^2. This behavior could be related to the absorption capability of the electrode at each wavelength.

The stability of the 6%(Fe, Ni)-60 ml photocathode for hydrogen production is investigated for an extended period of time in 0.3M Na$_2$SO$_4$ under simulated sunlight illumination and an applied voltage of -1V between the photocathode and the Pt counter electrode. The variation of the current density versus time is presented in Fig. 7d. As shown, the current density diminished sharply during the first 15 s to reach approximately 3.93 mA/cm^2. This sharp decrease in the current density can be attributed to a photocorrosion process that occurs between the photoelectrode and the redox electrolyte [47]. For times > 15 s, a limited increase in the current density is observed before reaching a constant value of about -4.14 mA / cm^2. This shows that despite the initial drop in photocurrent density, the 6%(Fe, Ni)-60 ml photoelectrode has high photochemical stability and a long lifetime as a photoelectrode in the PEC water splitting process for H$_2$ generation.
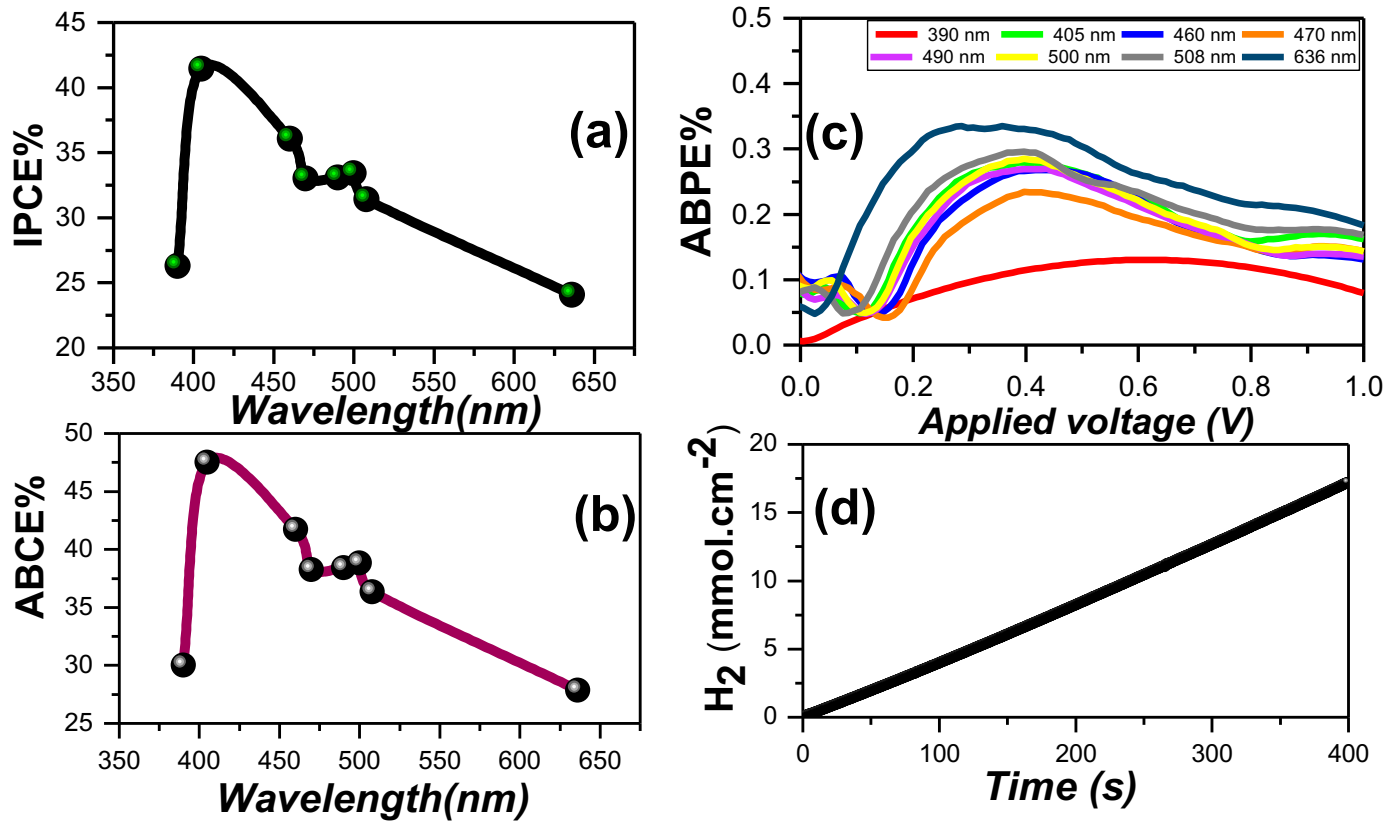
Fig. 8. (a) IPCE% and (b) ABCE% (λ) @-1V versus the incident wavelength, (c) ABPE% as a function of the applied potential at different wavelengths, and (d) the number of hydrogen moles versus generation time.

3.6.2. PEC efficiencies

The enhanced solar absorption of the 6%(Fe, Ni)-60 ml photoelectrode compared to our Co_3O_4, is confirmed by estimating the external quantum efficiency or incident photon-to-current efficiency (IPCE) at different wavelengths and fixed applied voltage (-1 V). The IPCE can be estimated using [75]:

$$IPCE= 1240.\frac{J_{ph}}{\lambda.P}. 100 \qquad (17)$$

where λ is the wavelength of the incident photons in nm, J_{ph} is the produced current density, p represents the power density of the illuminating light (100 mWcm^{-2}). The variation of IPCE with the wavelength of the monochromatic light is represented in Fig. 8a. The maximum value of IPCE is approximately 42% at 405 nm matching the maximum absorption as presented in Fig.2.

In the IPCE calculations, the effect of optical losses such as transmission(T) or reflection (R) of the incident photons has been neglected. To estimate the internal quantum efficiency which is also termed as the absorbed photon to current conversion efficiency (APCE) for correction of the optical losses. APCE is defined as the

number of photogenerated carriers that contribute to the obtained photocurrent per absorbed photon. APCE can be calculated using [76]:

$$APCE(\lambda) = \frac{IPCE(\lambda)}{A(\lambda)} = \frac{IPCE(\lambda)}{1-R-T} \qquad (18)$$

where A, R, T represent the optical absorption, reflection, and transmission, respectively.

Figure 8b shows the variation of APCE versus wavelength. As observed, the maximum APCE% value was 46% at 405 nm. As seen, the shape of the APCE curve is almost identical to the IPCE curve, this is because T and R are almost constant for 400-650 nm.

When a small external potential is applied to the PEC system, the electrical energy introduced into the system must be subtracted to evaluate the performance of the photoelectrode. or this, the applied bias photon to current conversion efficiency (ABPE) can be used. ABPE can be calculated using [41]:

$$ABPE(\%) = J_{ph}\frac{(1.23-V_{app})}{p} \times 100 \qquad (19)$$

where V_{app} is the externally applied bias. Figure 8c shows the variation of ABPE as a function of applied potential at different wavelengths. The maximum conversion efficiency under monochromatic illumination is 0.34%@-0.28V and 636 nm. Also, the 6%(Fe, Ni) photoelectrode displays an ABPE% of 0.110%@ 460 nm and 0V, which indicates the reduction of interfacial transport resistance and improving PEC performance. The photoelectrode's high response at low potential can be beneficial for PEC cell operation.

The solar- to- hydrogen conversion efficiency (STH), also called Benchmark efficiency, is defined as the ratio of the total hydrogen energy produced and the total sunlight energy put in (AM 1.5 G, 100 mWcm^2). It is considered as the overall efficiency of the PEC water splitting cell can be calculated using [77]:

$$STH = [(mmol\ H_2/S) \times (237\ KJ/mol)]/[P_{total}(mW/cm^2) \times A(cm^2)] \qquad (20)$$

where P_{total} is the total power density of the illuminating light, A represents the area of the illuminated part of the photoelectrode, H_2/S is the rate of the hydrogen production per second. The number of moles of hydrogen produced by the PEC- water splitting process was theoretically calculated using Faraday's law from equation (21)[75].

$$H_2(moles) = \int_0^t \frac{J_{ph}dt}{F} \qquad (21)$$

where F is the faraday constant (9.65×10^4 C mol^{-1}), and t is the time. The generated number of H_2 moles as a function of the generation time is shown in Fig. 8d. The rate of hydrogen production was 150 mmol h^{-1} cm^{-2}. Then, the estimated STH value was 11.37% for the 6%(Fe, Ni)-60 ml photoelectrode.

The optimized 6%(Fe, Ni)-60ml photoelectrode in this study showed higher current density and conversion efficiency than previously reported Co_3O_4-based PEC electrodes, as shown in table 3. For example, the PEC current density of Co_3O_4@Uio-66 and Co_3O_4/Ag were J_{ph}=10.2 mA.cm^{-2}@ 0.24 V_{RHE} in 2M KOH and J_{ph}= 4.73 mA.cm^{-2}@-0.4 V_{RHE} in 1M KOH, respectively[35, 78]. For Co_3O_4/BiVO$_4$ photocatalyst, the photoconversion efficiency was 0.659% @0.83 V_{RHE} in 1M Na$_2$SO$_3$ and IPCE% = 26%@360 nm in 0.5 MPBS [79, 80].

Table 3: Values of current density and conversion efficiency using our optimized photoelectrode and previously reported Co_3O_4 –based photocatalysts for PEC water splitting.

| Photoelectrode	Electrolyte	PEC performance	Ref
(Fe, Ni) codoped Co_3O_4	0.3M Na$_2$SO$_4$	J_{ph}=13.6 mA.cm^{-2}@ -1V, IPCE= 42% @405 nm, 150 mmol h^{-1} cm^{-2}	This work
Co_3O_4 nanosheet	0.5 M Na$_2$S	J_{ph}=33.6 µA/cm^2	[32]
Co_3O_4	0.1 M H$_2$SO$_4$	J_{ph}=1.15 mA.cm^{-2} @ 0.4 V_{RHE}, 34.4 µmol/L of hydrogen moles	[33]
Co_3O_4/Ag	1 M KOH	J_{ph}=4.73 mA.cm^{-2}@-0.4 V_{RHE} , IPEC% >22% at 300 nm	[35]
RGO-Co_3O_4	0.1 M H2SO$_4$	J_{ph}=0.75 mA.cm^{-2}@-0.35 V_{RHE}	[81]
Co-Pi/Co_3O_4/Ti:Fe$_2$O$_3$	1 M KOH	J_{ph}=2.7 mA.cm^{-2}@1.23 V_{RHE}, charge serpation efficiency =23% @1.23 V_{RHE}	[82]
Co_3O_4/BiVO$_4$	1M Na$_2$SO$_3$	J_{ph}=2.71 mA.cm^{-2} @1.23 V_{RHE}, photoconversion efficiency = 0.659% @0.83 V_{RHE}	[79]
Au/Co_3O_4/TiO$_2$	0.5 M Na$_2$SO$_3$	J_{ph}=0.37 mA.cm^{-2}@1.16 V_{RHE}	[83]
Co_3O_4/BiVO$_4$	0.5 MPBS (pH 7)	J_{ph}=2.35 mA.cm^{-2}@1.23 V_{RHE}, IPCE = 26%@360 nm, 0.61 mmol/cm^2	[80]
Ar/Co_3O_4/TiO$_2$	0.1 M NaOH	J_{ph}=2.5 mA.cm^{-2} @ 1.23 V_{RHE}, charge separation efficiency 90% @ 1.23 V_{RHE}	[84]
Co_3O_4@Uio-66	2 M KOH	J_{ph}=10.2 mA.cm^{-2}@ 0.24 V_{RHE}	[78]
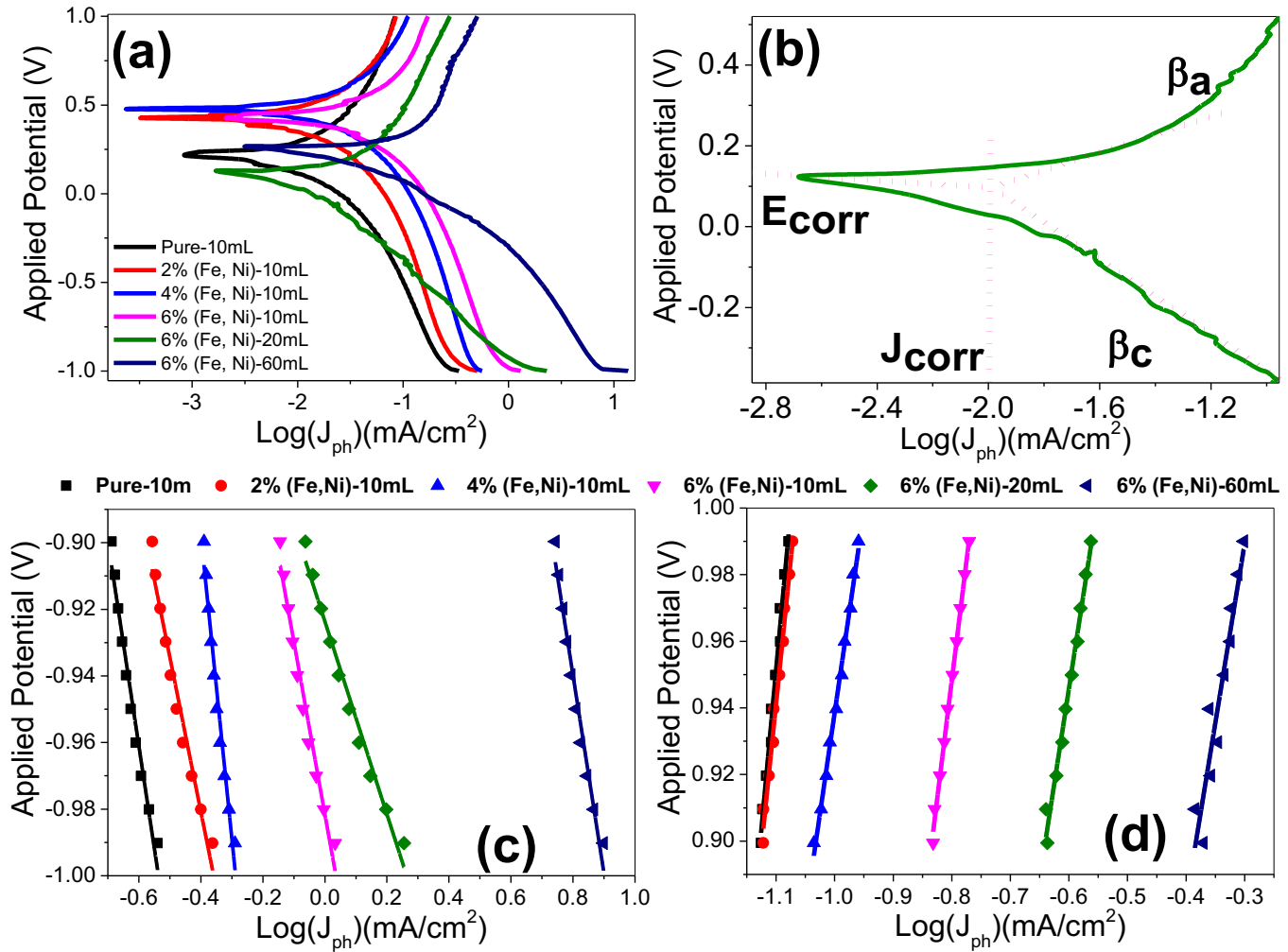
Fig. 9. Combined anodic and cathodic Tafel plots of (a) all deposited samples and (b)6%(Fe, Ni)-20 mL provided with the characteristic parameters; calculation of (c) cathodic slopes (βc) and (d) anodic slopes (βa).

3.7 Corrosion/Tafel parameters, and electrochemical surface area

To identify the mechanism of the HER process and identify the rate-limiting step, combined anodic and cathodic Tafel characteristics were measured using the to Tafel equation; $V=\beta \log(J_{ph}) + c$ [31]. Ideal photocatalysts have low Tafel slope values, high current-exchange rate, and thus, high HER performance. But this isn't an absolute rule, there are some photocatalysts with low Tafel slopes and also low current-exchange rate and vice versa [85]. Figure 9a shows the Tafel plots for all the deposited samples. Fig. 9b shows the main characteristic parameters; corrosion potential (E_{corr}), corrosion current (I_{corr}), anodic and cathodic Tafel slopes (β_a and β_c) for the 6%(Fe, Ni)-20 ml sample. The values of β_a and β_c for all electrodes were obtained from the slopes of the linear portions of the curves, as indicated in Fig.9c and Fig. 9d [86, 87]. The obtained values of

E_{corr}, I_{corr}, β_a, and β_c are displayed in Table 4 for all samples. The values of β_a and β_c decrease to 142.8 and 51.8 mV/dec, respectively, by increasing the codoping ratio from 2% to 6%. When the amount of sprayed solution was increased from 10 to 60 ml (all at 6%), the values for of β_a and β_c decreased further to 107.6 and 46.5 mV/dec, respectively. Tafel slopes indicate what the reaction mechanism and rate-limiting steps are in the PEC process. That is, when the recombination step is rate-limiting and the Tafel slope~30 mV/decade, the Volmer–Tafel mechanism is dominant. When PEC desorption is rate-limiting, and the Tafel slope ~40 mV/decade, the Volmer–Heyrovsky hydrogen evolution mechanism can be assumed dominant. If the Tafel slope~120 mV/decade, the reaction pathways depend on the surface filled with adsorbed hydrogen. The value βc indicates the over-potential required to increase the HGR rate by a factor 10 [86, 87]. For our samples, low Tafel slopes of the prepared photoelectrodes indicate that the energy of the bandgaps is low, resulting in low overpotentials due to the small amount of energy needed to achieve HGR performance and vice versa. Therefore, the 6% (Fe, Ni)-60ml and 6% (Fe, Ni)-10ml photoelectrodes showed the best values of βc and βa, explaining their high PEC performance compared to the other photoelectrodes.

E_{corr} only provides details about the solution's corrosion tendency, whereas the corrosion rate is proportional to I_{corr}. It can be seen in Fig.9 that the 6% co-doped samples present nobler behaviors. The 6%(Fe, Ni)-10mL has a higher E_{corr} (427 mV) in comparison with the 6%(Fe, Ni)-20mL and 6%(Fe, Ni)-60mL. This E_{corr} is also two folds that of the pure photoelectrode. The 6%(Fe, Ni)-20mL photoelectrode has the smallest corrosion potential (126 mV) of the photoelectrodes studied. Overall, the values of E_{corr} reported in this study are shifted to more noble behavior compared to commercial Co_3O_4 and higher than any previously reported data for Co_3O_4-based photoelectrodes [88].

The values of I_{corr}, polarization resistance (R_P), and corrosion rate (R) can be used to determine the photoelectrode's relative capability to resist corrosion. The CR is directly proportional and Rp is inversely proportional to the kinetic value I_{corr}. As shown in Table 4, 2%(Fe, Ni) incorporation decreases the corrosion current from 21.8 to 1.58 µA/cm². By increasing the codoping ratio to 6%, however, the corrosion current is increased to 5.52 µA/cm² but this is still much smaller than the pure photoelectrode's corrosion current. Increasing the deposited volume from 10mL to 60mL raises the corrosion current from 5.52 to 17.22 µA /cm², which could be associated with the rise in photoelectrode thickness from 771.57 to 2157.74 nm (see Table 1). The polarization resistance (R_p) in Ohm.cm² was estimated using Rp= βa βc / [2.303 I_{corr} (βa + βc)] based on the Stern-Geary equation and using a straight segment of the curves, close to E_{corr}. The corrosion rate (CR) was also estimated in nm/year using CR = 3272 I_{corr}[Ew/ A.d], where E_W , A, and d refer to equivalent weight (g/eq), area (cm²), and density (g/cm³). For all electrodes, the obtained Rp and CR values are listed in Table 4. The value of Rp increases from ~0.93 to 10.6 Ω.cm² and CR is reduced from 4.750 to 0.344 nm/year by adding 2%(Fe, Ni) to the pure photoelectrode. By increasing the codoping ratio to 6%, the CR is increased marginally to 1.20

nm/year, which is a quarter of the pure photoelectrode's corrosion rate. The values of the corrosion parameters mentioned indicate the great improvement of the photoelectrode's corrosion resistance through the implementation of optimized (Fe, Ni) codoping. This further demonstrates the significance of the (Fe, Ni) codoping in improving the stability of the electrode. The reported CR values are better than any previously reported Co_3O_4 based photoelectrode values [89]. This can be attributed to the higher Co^{2+}/Co^{3+} ratio (~0.98) observed from XPS measurements for 6% (Fe, Ni)-doped photoelectrode which is very high compared with pure Co3O4[62]. The main reason for the low PEC stability of pure CO_3O_4 is that the reduction potential of Co^{3+} is smaller than both the potential for H_2O reduction and the minimum of the conduction band, so that Co^{3+} can be reduced in the illuminated solution [90]. The decomposition of Co_3O_4 was observed by Tung et al., whereas CoO/Co_3O_4 showed high PEC stability for 1000 h under similar PEC water splitting conditions [91]. Yang et al. also demonstrated high PEC stability using a mixed-phase photoelectrode np^+-Si/CoOX ($Co_3O_4/Co_2O_3/CoO$) [92]. Co-based oxides are also widely used as a protective layer for PEC corrosion-resistant photoelectrodes.

Table 4. Corrosion and Tafel parameters, and ECSA values for the studied photoelectrodes.

Sample	E_{Corr} (V)	I_{Corr} ($\mu A/cm^2$)	βa (mV/dec)	βc (mV/dec)	Rp (Ohm.cm^2)	Corr Rate (nm/year)	ECSA (m^2/g)
Pure-10mL	0.216	21.80	190.5±8.6	61.6±2.3	0.9284	4.75	15.351
2%(Fe, Ni)-10mL	0.427	1.58	172.4±6.9	49.4±2.9	10.5662	34.40	18.517
4%(Fe, Ni)-10mL	0.477	2.47	120.9±3.5	80.2±5.3	8.4872	53.78	26.598
6%(Fe, Ni)-10mL	0.427	5.52	142.8±2.6	51.8±3.1	2.9940	1.20	46.940
6%(Fe, Ni)-20mL	0.126	8.83	114.0±4.8	30.3±1.4	1.1787	1.92	26.664
6%(Fe, Ni)-60mL	0.267	17.22	107.6±12.2	46.5±3.2	0.8198	3.75	73.005

The electrochemical surface area (ECSA) of the prepared photoelectrodes was calculated based on the Randles-Sevcik relationship, ECSA1= $I(R\ T)^{0.5} (C\ n\ F)^{-1.5}(v\ D)^{-0.5}/0.4463$, wherever n, F, C, R, T, and D refer to the number of electrons in the redox reactions (here n=1), Faraday constant, analyte concentration, gas-molar constant, temperature, and analyte-diffusion constant respectively [86]. Using Fig. 7a, the ECSA values of the photoelectrodes were obtained by ECSA= Q/(m. C), where Q, m, and C are the negative-scan hydrogen-adsorption charges after double-layered charges modification, catalyst mass and complete monolayer charges of the photoelectrode-covering H-atoms, respectively [86]. The Q values were obtained by integrating the curves of each photoelectrode divided by the measurements-scanning-rate (10 mV) in Fig. 7a. The ECSAs for the photoelectrodes were determined and presented in Table 4. For the pure-10mL, 6%(Fe, Ni)-10 mL, and 6% (Fe,

Ni)-60 mL, the values were 15.4, 46.9 and 73.0 m²/g, respectively. The high ECSA can explain the high PEC performance for the 6% (Fe, Ni)-60 mL photoelectrode compared to the other photoelectrodes.
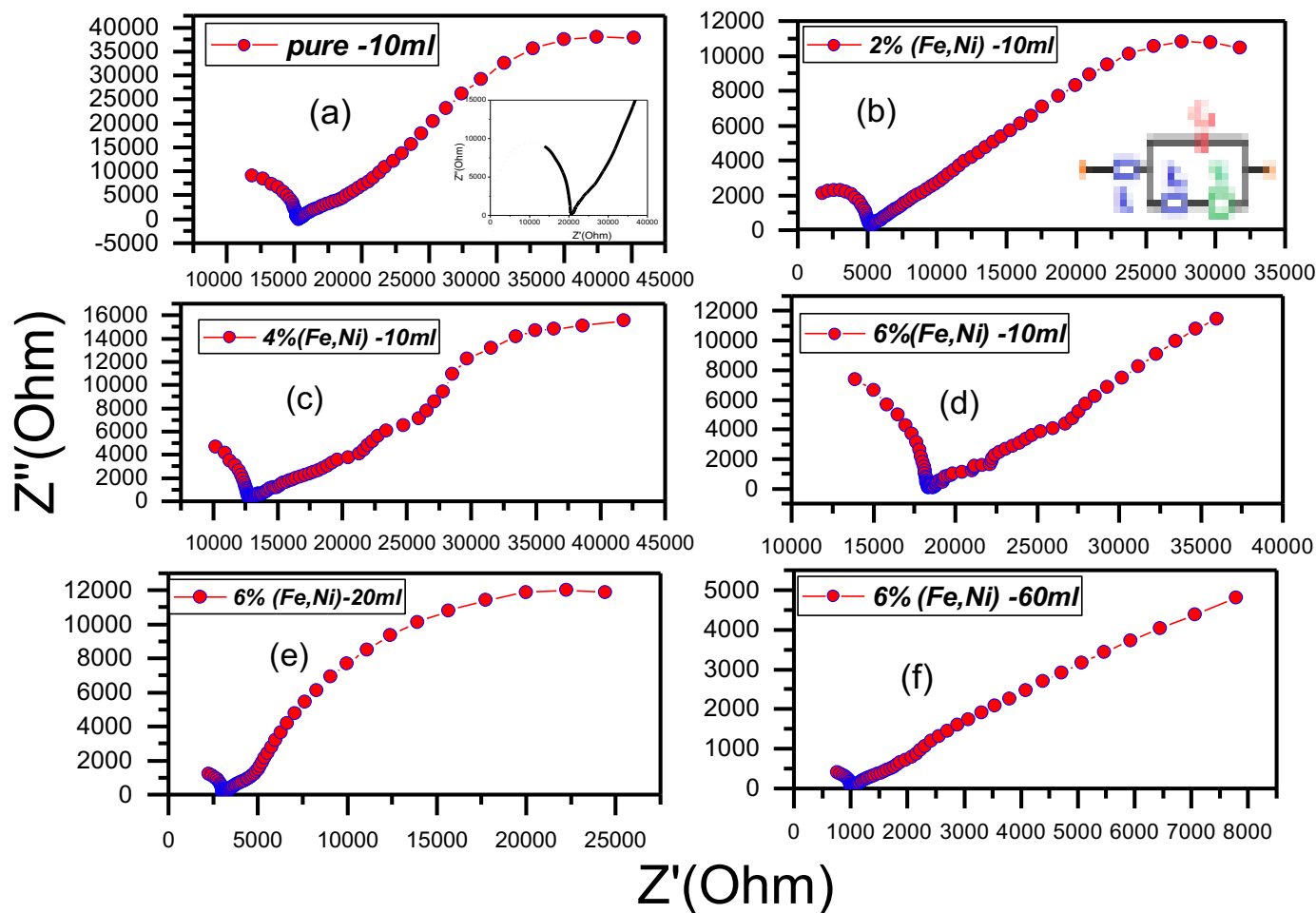

Fig. 10. Nyquist plots for pure and (Fe, Ni) codoped Co_3O_4 photoelectrodes in 0.3 M Na_2SO_4 electrolyte at 0V (vs Ag/AgCl) and under white light illumination.

3.8. Electrochemical impedance spectroscopy (EIS):

Charge carrier dynamics play an important role in determining the photocatalytic efficiency of photoelectrodes in the PEC water splitting process. To investigate the charge carrier dynamics of the deposited photoelectrodes, EIS measurements were performed at room temperature using an electrochemical workstation (CH Instruments CHI660E). The undoped and (Fe, Ni)-codoped Co_3O_4 photoelectrodes were immersed in 0.3 M Na_2SO_4 electrolyte and the EIS measurements were carried out for a frequency range of 0.01-100,000 Hz at 0V (vs Ag/AgCl) under illumination. The Nyquist plots for all photoelectrodes are displayed in Fig.10. All photoelectrodes exhibited a semicircle at high frequencies due to charge transfer processes in electrode/electrolyte boundaries (charge transfer resistance) and two straight line segments observed at low frequencies with slopes ~45° and ~55° due to diffusion-controlled processes (Warburg impedance) and additional limited capacitive behavior (double-layer capacitance) as shown in the inset of Fig. 10a. I.e, the EIS

data illustrates mixed diffusion and kinetic controlled routes. To understand the EIS measurements through hydrogen evolution, the obtained results are fitted to a simple equivalent circuit. The inset of Fig. 10b shows the Randle equivalent circuit that was used to simulate the EIS data using the ZSimpWin software. This equivalent circuit consists of electrolyte resistance (Rs) that can be obtained from Nyquist plot intercepts at high frequencies, charge transfer resistance (Rct) equal to the semicircle diameter in the Nyquist plot, double-layer capacitance (C_{dl}) and Warburg impedance (W). The numerical values obtained for these elements provided with the fitting error are presented in Table 5 for all photoelectrodes. Both 6% (Fe, Ni)-20ml and 6% (Fe, Ni)-60ml photoelectrodes have the lowest Rs and Rct values compared to the other samples, promoting the PEC hydrogen production. The smallest value for Rct was for 6% (Fe, Ni)-60ml photoelectrode (0.84 Ω). This Rct value is much smaller than any literature value for Co_3O_4-based PEC electrodes [93-95].

Figure S2 (supplementary data) presents Bode plots for all the photoelectrodes, measured at room temperature using 0.3 M Na_2SO_4 at 0 V (vs Ag/AgCl). Fig. S2a shows the variation of the total impedance (Z) with the frequency, whilst Fig. S2b shows the variation of the phase with the logarithm of the frequency. Figure S2a shows a resistive regime related to the R_{ct} at low frequencies in addition to a capacitive contribution related to the C_{dl} of the electrode at high frequencies [87]. From Fig. S2b, the maximum phase shift (Θ_{max} in degree), and the frequency at the maximum phase (f_{max} in Hz), are estimated and displayed in Table 5 for all photoelectrodes. By increasing the codoping ratio from 0% to 6%@10mL, the Θ_{max} is decreased from 32.8º to 17.7º, whereas the rise in photoelectrode thickness from 771.57 to 2157.74 nm increases the Θ_{max} from 17.7º to 32.1º. The lifetime of the charge carriers can be estimated from Fig. S2b via the relationship $\tau_n = 1/2\pi f_{max}$ [96]. The obtained values for all electrodes are shown in Table 5. The lifetime of the charge carriers is almost doubled by increasing the codoping ratio from 0% to 6%@10mL. The obtained parameters from Figs.10 and S2 indicate a great reduction in the charge recombination at the electrolyte/electrode interfaces with increasing doping level. This also refers to a kinetically facile PEC system, improved ionic conductivity and electrolytes diffusion through the 6% (Fe, Ni)-60ml photoelectrode. Therefore, this photoelectrode showed higher photocatalytic performance to produce large amounts of H_2 compared to the other photoelectrodes.

Table 5: The numerical values of the Randle circuit elements obtained from EIS measurements for all

Photoelectrodes.

| Photolectrode	R_s/ Ω	R_{ct}/ Ω	C_{dl} /F $\times 10^{-10}$	W $\times 10^{-4}$	Fitting error	Θ_{max} / degree	f_{max} /Hz	τ_n/sec
pure-10mL	2.902	17.80	0.718	0.639	1.17×10^{-8}	32.8°	0.018	8.84
2%(Fe,Ni)-10ml	0.917	4.65	6.684	1.189	1.53×10^{-8}	23.1°	0.026	6.12
4%(Fe,Ni)-10mL	5.957	7.65	2.020	1.088	6.53×10^{-4}	22.9°	0.022	7.23
6%(Fe,Ni)-10mL	4.800	14.09	0.872	1.786	0.05	17.7°	0.010	15.91
6%(Fe,Ni)-20mL	0.813	2.27	5.542	1.898	0.06	37.7°	0.046	3.46
6%(Fe,Ni)-60mL	0.190	0.84	13.000	40.722	2.5×10^{-8}	32.1°	0.018	8.84
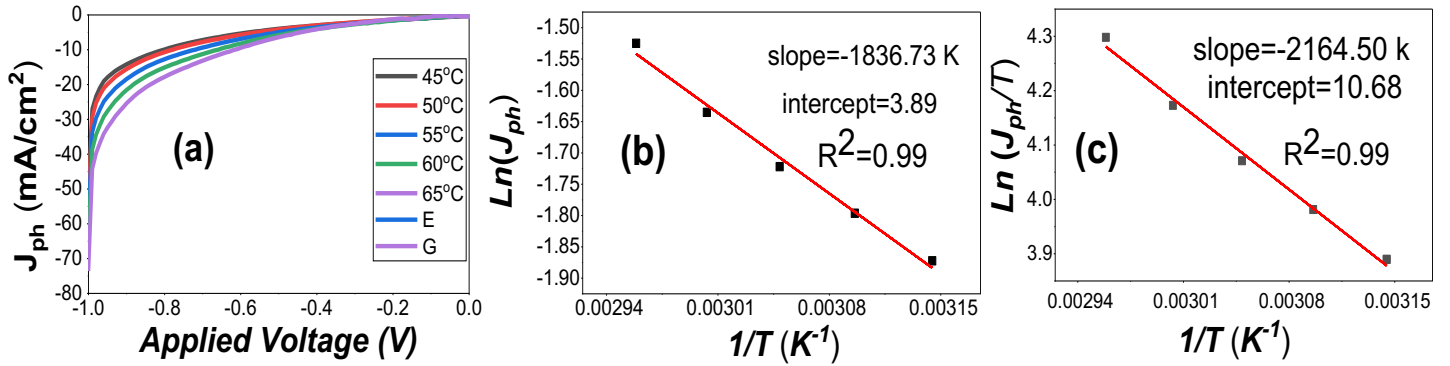
Fig. 11. (a) the variation of J_{ph}-V characteristics at different temperatures, (b) ln(J_{ph}) versus (1/T), and (c) Ln(J_{ph}/T) versus (1/T).

3.9. Effect of temperature and thermodynamic parameters

Figure 11 shows the effect of temperature, 45 to 65 °C, on the PEC current density (J_{ph}) of the 6%(Fe, Ni)-60ml photoelectrode. The current density is increased from 13.6 mA/cm² to 75 mA/cm² by increasing the temperature to 65°C. The increase of the current density with the increase in temperature can be explained as follows: (i) Increasing the temperature of the photogenerated carriers will increase the concentration of electrons in the conduction band and holes in the valence band, increasing the rate of redox reactions and current density. (ii) Increasing the temperature will increase the mobility of the charge carrier and thus the lifetime of the carrier according to the relationship µ= qτ_n /m*, where µ represents the mobility of the carrier, and m* is the effective mass of the charge carrier. This leads to a decrease in the recombination rate of the carriers generated and improves the process of hydrogen generation.

From the J_{ph}-V curves at different temperatures shown in Fig. 11a, thermodynamic parameters such as activation energy(E_a), entropy (Δs^*), and enthalpy (ΔH^*) can be derived. The activation energy of the reaction is determined from the slope of the linear fitting of the variation of $\ln(J_{ph})$ versus $1/T$ using the following Arrhenius equation[97]:

$$k = A\,e^{\frac{-E_a}{RT}} \tag{22}$$

where k represents the rate constant, R is the universal gas constant (8.314472 J.K^{-1}.mol^{-1}), T is the absolute temperature in Kelvin. From the slope of the linear fitting of Fig. 11b, slope = $-E_a/R$, the activation energy is found to be approximately 15.27 kJ.mol^{-1}. The values of Δs^* and ΔH^* of the reaction were calculated using the Eyring equation by plotting a relation between $Ln(J_{ph}/T)$ versus $(1/T)$ as shown in Fig. 11c. The Eyring equation can be expressed as [97]:

$$k = \frac{TK_B}{h}\,.e^{\frac{\Delta S^*}{R}}.e^{\frac{-\Delta H^*}{TR}} \tag{23}$$

where K_B is the Boltzmann's constant (1.38×10^{-23} J.K^{-1}), and h is the Planck's constant (6.626×10^{-34} J.S). From the slope of the linear fitting, the value of ΔH^* is found to be 17.99 kJ.mol^{-1} and from the intercept, the value of Δs^* is found to be -108.75 Jmol^{-1}K^{-1}.

3.10. Suggested PEC Mechanism for H$_2$ production

A simple PEC mechanism is illustrated in Fig. 12. It illustrates bandgap diagrams for (a) pure and (b) 6%(Fe, Ni) codoped Co_3O_4-10mL photoelectrodes using the values of E_{gI} and E_{gII} from Table 2. The difference between E_{gI} and E_{gII} is 1.15 eV for the pure Co_3O_4 and 1.51 eV for the codoped Co_3O_4 photoelectrode. The addition of (Fe, Ni) to Co_3O_4 lowers the E_{gI} and extends E_{gII} over a wide range of the incident photon, making the 6%(Fe, Ni) codoped Co_3O_4-10mL sample a promising photocatalytic electrode to enhance the PEC. An incident photon of appropriate wavelength excites an electron from the VB to the CB, where the applied potential allows electron-hole separation. The addition of (Fe, Ni) to Co_3O_4 increases the charge carriers' lifetime and mobility upon irradiation by reducing recombination. This means that for the (Fe, Ni)codoped Co_3O_4 electrode surfaces there is reduced e$^-$-h$^+$ recombination leading to a lower necessary potential for the PEC water splitting. The H$_2$ generation can occur as illustrated in Fig. 12c by transferring the free electrons to H$_2$O molecules. The codoping with (Fe, Ni) increases the efficiency of hydrogen production through three key points: the increase of the photons mean path through the dispersion of the light in addition to the multiple reflections inside the nanostructured surface attributable to the variability of the ionic radii of Co, Fe, and Ni; near-field enhancement by the release and transmission of high-energy photons or active charge carriers to the surfaces; and electron excitations to CB levels above the Fermi level by overcoming the Schottky barriers [91, 98]. On the other side, the Na$_2$SO$_4$ molecules, with the assistance of OH$^-$, accept holes from (Fe, Ni) codoped

Co₃O₄ electrode for O₂ generation at the Pt counter electrode. I.e., the generated electrons reduce H_2O molecules while interacting with hydrogen ions to create hydrogen atoms ($4H^+ + 4e^- \rightarrow 2H_2$ ($E^o_{H+/H2}$ = +0.00 V_{NHE})), whereas the water oxidation occurs at the Pt-electrode that serves as an anode for the PEC cell ($2H_2O + 4h^+ \rightarrow 4H^+ + O$ ($E^o_{H2O/O2}$ = -1.229 V_{NHE})). Codoping with (Fe, Ni) also greatly improves PEC efficiency because of the passivation of surface states, charge carriers' concentration enhancement, and charge mobility improvement. This output results from bending and extending the band through the entire region of (Fe, Ni) codoped electrode, thus enhancing the separation of the charge carriers. Eventually, the PEC hydrogen generation cell must allow area-saving assembly with a limited number of low-cost components (wires, photoelectrodes, vessels, etc.); the cost of the 6% (Fe, Ni) co-doped electrode is estimated to be approximately US$ 1.40 per (3 cm x 3 cm) electrode, which could be reduced to US$ 1-1.20 for large industrial production. In conclusion, this study shows that (Fe, Ni) codoped Co3O4 is a very promising candidate for use as high-performance PEC electrodes providing excellent efficiency, good lifetime, and production at a reasonable cost.
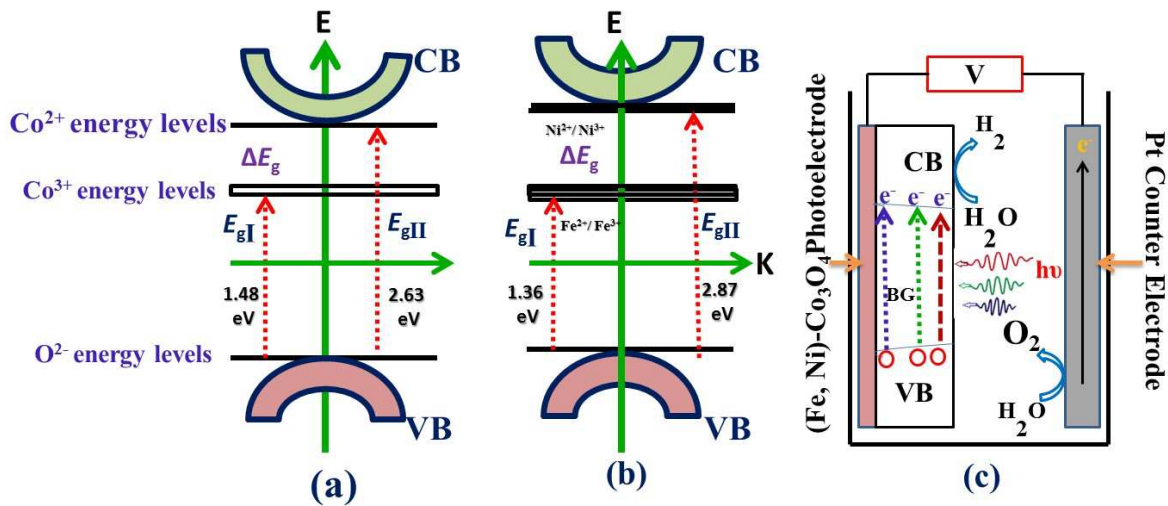
Fig. 12. Bandgap diagram of (a) pure and (b) 6% (Fe, Ni) Co₃O₄-10 mL, and (C) schematic diagram of PEC water splitting using (Fe, Ni) Co₃O₄ photoelectrode.

4. Conclusion

Pure and (Fe, Ni) co-doped Co₃O₄ photoelectrodes of different codoping ratios and thicknesses have been successfully deposited on glass substrates at 450°C using a homemade spray pyrolysis technique. The chemical composition, crystallographic structure, optical and electrical properties of all photoelectrodes were investigated. The grain size decreases from 30.60 nm to 12.02 nm by incorporating 6% (Fe, Ni) codoping. The thickness of the 6% codoped electrode is increased from 771.57 nm to 2157.74 nm by increasing the sprayed volume from 10 mL to 60 mL. The photoelectrochemical (PEC) properties of the prepared photoelectrodes were investigated and optimized towards efficient solar light-driven hydrogen production. Among the studied photoelectrodes, the 6%(Fe, Ni)-60ml Co₃O₄ photoelectrode displays a photocatalytic hydrogen output rate of

150 mmol h^{-1}/cm^2 @-1V in 0.3M Na$_2$SO$_4$ electrolyte. The highest photocurrent density reached up to 13.6 mA/cm^2@-1V with IPCE = 42% @405 nm, STH = 11.37% for 6%(Fe, Ni)-60ml Co$_3$O$_4$ photoelectrode , which are the highest values yet for Co$_3$O$_4$-based photoelectrodes. The value of ABPE% is 0.34%@ -0.28V and 636 nm. This photoelectrode displays a photogenerated current density of -0.14 mA cm^{-2} @ 0 V and PEC current onset over 0.266 V. As the PEC reaction temperature increases to 65 °C the current density increases to 75 mA.cm^{-2}. The thermodynamic parameters were also estimated for the 6% (Fe, Ni)-60ml PEC electrode; activation energy= 15.27kJ.mol^{-1}, entropy=108.75 Jmol^{-1}K^{-1}, and enthalpy= 17.99 kJ.mol^{-1}. Furthermore, this co-doped photoelectrode showed the highest PEC surface area (~ 5 folds the pure sample) and the lowest Tafel slopes (107.6 and 46.5 mv/dec). Moreover, the lifetime of the charge carriers was almost doubled and the corrosion rate was reduced from 4.75 to 1.20 nm/year by increasing the codoping ratio from 0% to 6%@10mL, which indicates to a great reduction in the charge recombination at electrolyte/electrode interfaces. These parameters were used to identify the production mechanism of PEC H$_2$, in addition to the stability and reusability tests. This study not only shows a simple and transparent technique to develop a new collection of high-quality PEC photoelectrodes but also provides a new perspective for enhancing PEC hydrogen generation efficiency under sunlight illumination.

Competing Interests: The authors declare that there are no competing interests.

Author Contribution: **Alhoda Abdelmoneim:** Methodology, Investigation, Resource, Writing - Original Draft. **Ahmed Naji:** Conceptualization, Methodology, Validation, Investigation, Resources, Writing - Original Draft, Writing - Review & Editing, Supervision. **Erik Wagenaars:** Writing - Review & Editing. **Mohamed Shaban:** Conceptualization, Methodology, Validation, Investigation, Resources, Writing - Original Draft, Writing - Review & Editing, Project administration, Supervision.

Data Availability: The raw data required to reproduce these findings are available from the corresponding author, upon reasonable request. The processed data required to reproduce these findings are available from the corresponding author, upon reasonable request.

References

1. Minggu, L.J., W.R.W. Daud, and M.B. Kassim, *An overview of photocells and photoreactors for photoelectrochemical water splitting.* International journal of hydrogen energy, 2010. **35**(11): p. 5233-5244.
2. Marchal, C., et al., *Au/TiO 2 photocatalysts prepared by solid grinding for artificial solar-light water splitting.* New Journal of Chemistry, 2016. **40**(5): p. 4428-4435.
3. Ahmad, H., et al., *Hydrogen from photo-catalytic water splitting process: A review.* Renewable and Sustainable Energy Reviews, 2015. **43**: p. 599-610.

4.   Khatri, N. and S. Tyagi, *Influences of natural and anthropogenic factors on surface and groundwater quality in rural and urban areas.* Frontiers in Life Science, 2015. **8**(1): p. 23-39.

5.   Dashtian, K., et al., *Achieving enhanced blue-light-driven photocatalysis using nanosword-like VO2/CuWO4 type II n–n heterojunction.* Chemical Engineering Journal, 2018. **339**: p. 189-203.

6.   Maeda, K. and K. Domen, *Photocatalytic Water Splitting: Recent Progress and Future Challenges.* The Journal of Physical Chemistry Letters, 2010. **1**(18): p. 2655-2661.

7.   Akkerman, I., et al., *Photobiological hydrogen production: photochemical efficiency and bioreactor design.* International Journal of Hydrogen Energy, 2002. **27**(11): p. 1195-1208.

8.   Bu, Y. and J.-P. Ao, *A review on photoelectrochemical cathodic protection semiconductor thin films for metals.* Green Energy & Environment, 2017. **2**(4): p. 331-362.

9.   Joy, J., J. Mathew, and S.C. George, *Nanomaterials for photoelectrochemical water splitting–review.* international journal of hydrogen energy, 2018. **43**(10): p. 4804-4817.

10.   Bak, T., et al., *Photo-electrochemical hydrogen generation from water using solar energy. Materials-related aspects.* International journal of hydrogen energy, 2002. **27**(10): p. 991-1022.

11.   Zhang, J.Z., *Metal oxide nanomaterials for solar hydrogen generation from photoelectrochemical water splitting.* MRS bulletin, 2011. **36**(1): p. 48-55.

12.   Wang, G., Y. Ling, and Y. Li, *Oxygen-deficient metal oxide nanostructures for photoelectrochemical water oxidation and other applications.* Nanoscale, 2012. **4**(21): p. 6682-6691.

13.   Wang, G., et al., *Hydrogen-treated TiO2 nanowire arrays for photoelectrochemical water splitting.* Nano letters, 2011. **11**(7): p. 3026-3033.

14.   Peerakiatkhajohn, P., et al., *Stable hematite nanosheet photoanodes for enhanced photoelectrochemical water splitting.* Advanced Materials, 2016. **28**(30): p. 6405-6410.

15.   Kang, Z., et al., *Interface engineering for modulation of charge carrier behavior in ZnO photoelectrochemical water splitting.* Advanced Functional Materials, 2019. **29**(15): p. 1808032.

16.   Wang, Y., et al., *Tungsten trioxide nanostructures for photoelectrochemical water splitting: material engineering and charge carrier dynamic manipulation.* Advanced Functional Materials, 2019. **29**(23): p. 1809036.

17.   Manogowri, R., et al., *Effect of annealing temperature on the structural, morphological, optical and electrical properties of Co 3 O 4 thin film by nebulizer spray pyrolysis technique.* Journal of Materials Science: Materials in Electronics, 2016. **27**(4): p. 3860-3866.

18.   Ansari, A.R., et al., *Synthesis, characterization and oxidation of metallic cobalt (Co) thin film into semiconducting cobalt oxide (Co3O4) thin film using microwave plasma CVD.* Materials Research Express, 2018. **5**(6): p. 065003.

19.   Aboud, A.A., et al., *Characterization of nano-crystalline Co-La mixed oxide thin films prepared by the spray pyrolysis technique.* Results in Physics, 2019. **12**: p. 1513-1519.

20.   Elhag, S., et al., *Synthesis of Co3O4 cotton-like nanostructures for cholesterol biosensor.* Materials, 2015. **8**(1): p. 149-161.

21.   Patil, V., et al., *New Method for Fabrication of Co^ sub 3^ O^ sub 4^ Thin Film Sensors: Structural, Morphological and Optoelectronic Properties.* Sensors & Transducers, 2011. **128**(5): p. 100.

22.   Cheong, J.Y., et al., *High-rate formation cycle of Co3O4 nanoparticle for superior electrochemical performance in lithium-ion batteries.* Electrochimica Acta, 2019. **295**: p. 7-13.

23.   Akhtar, M.A., A. Chowdhury, and A. Chandra, *Addition of redox additives—synergic strategy for enhancing the electrochemical activity of spinel Co3O4 based supercapacitors.* Journal of Physics D: Applied Physics, 2019. **52**(15): p. 155501.

24.   Lou, X., et al., *Synthesis and photocatalytic property of Co3O4 nanorods.* Materials Science and Engineering: B, 2007. **137**(1-3): p. 268-271.

25.   Barrera, E., et al., *Cobalt oxide films grown by a dipping sol-gel process.* Thin Solid Films, 1999. **346**(1-2): p. 138-144.

26.   Bahlawane, N., et al., *Characterization and tests of planar Co3O4 model catalysts prepared by chemical vapor deposition.* Applied Catalysis B: Environmental, 2004. **53**(4): p. 245-255.

27.   Kayani, Z.N., et al., *Preparation and characterization of dip coated cobalt oxide thin films.* Materials Research Innovations, 2019. **23**(5): p. 253-259.

28.   Matsuda, A., et al., *Room-temperature selective epitaxial growth of CoO (1 1 1) and Co3O4 (1 1 1) thin films with atomic steps by pulsed laser deposition.* Applied Surface Science, 2015. **349**: p. 78-82.

29. Prieto, P., et al., *Highly oriented (111) CoO and Co3O4 thin films grown by ion beam sputtering.* Journal of Alloys and Compounds, 2019. **810**: p. 151912.

30. Patel, M. and J. Kim, *Thickness-dependent photoelectrochemical properties of a semitransparent Co3O4 photocathode.* Beilstein Journal of Nanotechnology, 2018. **9**(1): p. 2432-2442.

31. Patel, M., et al., *Photoelectrocatalytic sea water splitting using Kirkendall diffusion grown functional Co3O4 film.* Solar Energy Materials and Solar Cells, 2017. **171**: p. 267-274.

32. Mao, Y., et al., *Topotactic transformation to mesoporous Co3O4 nanosheet photocathode for visible-light-driven direct photoelectrochemical hydrogen generation.* Materials Letters, 2014. **134**: p. 276-280.

33. Moridon, S.N.F., et al., *Cobalt oxide as photocatalyst for water splitting: Temperature-dependent phase structures.* International Journal of Hydrogen Energy, 2019. **44**(47): p. 25495-25504.

34. Zhang, Y., et al., *Enhancing photocatalytic oxygen evolution activity of cobalt-based spinel nanoparticles.* Catalysis Today, 2014. **225**: p. 171-176.

35. Hong, T., et al., *Efficient photoelectrochemical water splitting over Co3O4 and Co3O4/Ag composite structure.* Applied Catalysis B: Environmental, 2017. **202**: p. 454-459.

36. Ebadi, M., et al., *Electrodeposited p-type Co 3 O 4 with high photoelectrochemical performance in aqueous medium.* RSC Advances, 2015. **5**(46): p. 36820-36827.

37. Dholam, R., et al., *Hydrogen production by photocatalytic water-splitting using Cr-or Fe-doped TiO2 composite thin films photocatalyst.* International Journal of Hydrogen Energy, 2009. **34**(13): p. 5337-5346.

38. Gasparotto, A., et al., *F-Doped Co3O4 Photocatalysts for Sustainable H2 Generation from Water/Ethanol.* Journal of the American Chemical Society, 2011. **133**(48): p. 19362-19365.

39. Singh, P., R. Kumar, and R.K. Singh, *Progress on transition metal-doped ZnO nanoparticles and its application.* Industrial & Engineering Chemistry Research, 2019. **58**(37): p. 17130-17163.

40. Abbas, S., et al. *Effect of substrate temperature on structure and optical properties of Co3O4 films prepared by spray pyrolysis technique*. in *IOP Conference Series: Materials Science and Engineering*. 2014. IOP Publishing.

41. Aboud, A.A., M. Shaban, and N. Revaprasadu, *Effect of Cu, Ni and Pb doping on the photo-electrochemical activity of ZnO thin films.* RSC Advances, 2019. **9**(14): p. 7729-7736.

42. Jogade, S., et al., *MOCVD of cobalt oxide using co-actylacetonate as precursor: Thin film deposition and study of physical properties.* 2011.

43. Aboud, A.A., et al., *The effect of Cu-doping on CdS thin films deposited by the spray pyrolysis technique.* Journal of Materials Research and Technology, 2019. **8**(2): p. 2021-2030.

44. Jongnavakit, P., et al., *Preparation and photocatalytic activity of Cu-doped ZnO thin films prepared by the sol–gel method.* Applied Surface Science, 2012. **258**(20): p. 8192-8198.

45. Mariappan, R., et al., *Structural, Optical and Electrical Properties of Thin Films Using Nebulizer Spray Pyrolysis Technique.* Indian Journal of Materials Science, 2013. **2013**.

46. Hassan, A.I. and S.I. Maki, *INTERNATIONAL JOURNAL OF ENGINEERING SCIENCES & RESEARCH TECHNOLOGY STRUCTURAL AND OPTICAL PROPERTIES OF COPPER-DOPED COBALT OXIDE THIN FILMS PREPARED BY SPRAY PYROLYSIS.*

47. Zayed, M., A.M. Ahmed, and M. Shaban, *Synthesis and characterization of nanoporous ZnO and Pt/ZnO thin films for dye degradation and water splitting applications.* International Journal of Hydrogen Energy, 2019.

48. Jogade, S., D. Sutrave, and V. Patil, *Structural and Morphological Properties of Mn-Doped Co3O4 Thin Film Deposited by Spin Coat Method.* IJERA, 2016. **6**(9): p. 42-46.

49. Krishnamachari, N. and C. Calvo, *Crystallographic studies of cobalt arsenates II. Crystal structure of Co8As3O16.* Canadian Journal of Chemistry, 1970. **48**(20): p. 3124-3131.

50. Pandey, B., et al., *Structures, bonding and reactivity of iron and manganese high-valent metal-oxo complexes: A computational investigation.* Journal of Chemical Sciences, 2015. **127**(2): p. 343-352.

51. Walch, S.P. and W. Goddard III, *Electronic States of the NiO Molecule1y2.*

52. Pourrahimi, A.M., et al., *Water-based synthesis and cleaning methods for high purity ZnO nanoparticles–comparing acetate, chloride, sulphate and nitrate zinc salt precursors.* RSC Advances, 2014. **4**(67): p. 35568-35577.

53. Moss, T., *Optical Properties of Semiconductors [Russian translation].* IL, Moscow, 1961: p. 154.

54. Gençyılmaz, O., et al., *Synthesis, characterization and ellipsometric study of ultrasonically sprayed Co 3 O 4 films.* Applied Physics A, 2015. **121**(1): p. 245-254.

55.   Shaban, M., M. Mustafa, and A. El Sayed, *Structural, optical, and photocatalytic properties of the spray deposited nanoporous CdS thin films; influence of copper doping, annealing, and deposition parameters.* Materials Science in Semiconductor Processing, 2016. **56**: p. 329-343.

56.   Venkatesh, R., et al., *Analysis of optical dispersion parameters and electrochromic properties of manganese-doped Co3O4 dendrite structured thin films.* Journal of Physics and Chemistry of Solids, 2018. **122**: p. 118-129.

57.   Greczynski, G. and L. Hultman, *In-situ observation of self-cleansing phenomena during ultra-high vacuum anneal of transition metal nitride thin films: Prospects for non-destructive photoelectron spectroscopy.* Applied Physics Letters, 2016. **109**(21): p. 211602.

58.   Barr, T.L. and S. Seal, *Nature of the use of adventitious carbon as a binding energy standard.* Journal of Vacuum Science & Technology A: Vacuum, Surfaces, and Films, 1995. **13**(3): p. 1239-1246.

59.   Wang, Z., et al., *Surface oxygen vacancies on Co 3 O 4 mediated catalytic formaldehyde oxidation at room temperature.* Catalysis Science & Technology, 2016. **6**(11): p. 3845-3853.

60.   Gallant, D., M. Pezolet, and S. Simard, *Optical and physical properties of cobalt oxide films electrogenerated in bicarbonate aqueous media.* The Journal of Physical Chemistry B, 2006. **110**(13): p. 6871-6880.

61.   Li, J., et al., *Ultrathin mesoporous Co3O4 nanosheet arrays for high-performance lithium-ion batteries.* ACS Omega, 2018. **3**(2): p. 1675-1683.

62.   Pocoví-Martínez, S., I. Zumeta-Dube, and D. Diaz, *Production of Methanol from Aqueous CO2 by Using Co3O4 Nanostructures as Photocatalysts.* Journal of Nanomaterials, 2019. **2019**.

63.   Wu, H., et al., *Co 2+/Co 3+ ratio dependence of electromagnetic wave absorption in hierarchical NiCo 2 O 4– CoNiO 2 hybrids.* Journal of Materials Chemistry C, 2015. **3**(29): p. 7677-7690.

64.   Niu, G., et al., *Oxygen doping in nickel oxide for highly efficient planar perovskite solar cells.* Journal of Materials Chemistry A, 2018. **6**(11): p. 4721-4728.

65.   Won, J., et al., *Physicochemical Modification Effect on Homogeneously Aligned Liquid Crystals Based on the Nickel Oxide Thin Film.* Journal of nanoscience and nanotechnology, 2019. **19**(10): p. 6139-6143.

66.   Park, J.-S., J.S. Cho, and Y.C. Kang, *Scalable synthesis of NiMoO4 microspheres with numerous empty nanovoids as an advanced anode material for Li-ion batteries.* Journal of Power Sources, 2018. **379**: p. 278-287.

67.   Yamashita, T. and P. Hayes, *Analysis of XPS spectra of Fe2+ and Fe3+ ions in oxide materials.* Applied surface science, 2008. **254**(8): p. 2441-2449.

68.   Akshay, V., et al., *Significant reduction in the optical band-gap and defect assisted magnetic response in Fe-doped anatase TiO 2 nanocrystals as dilute magnetic semiconductors.* New Journal of Chemistry, 2019. **43**(15): p. 6048-6062.

69.   Ghosh, B., et al., *Tuning of magnetic behaviour in nitrogenated graphene oxide functionalized with iron oxide.* Diamond and Related Materials, 2018. **89**: p. 35-42.

70.   Song, W., *Synthesis and Characterization of Transition Metal Oxide Catalysts for Environmental and Energy Storage Applications.* 2016.

71.   Shinde, V., et al., *Supercapacitive cobalt oxide (Co3O4) thin films by spray pyrolysis.* Applied Surface Science, 2006. **252**(20): p. 7487-7492.

72.   Pearson, G.L. and J. Bardeen, *Electrical properties of pure silicon and silicon alloys containing boron and phosphorus.* Physical Review, 1949. **75**(5): p. 865.

73.   Tareen, J., et al., *Growth and electrical properties of pure and Ni-doped Co3O4 single crystals.* Materials research bulletin, 1984. **19**(8): p. 989-997.

74.   Manickam, M., et al., *Structural, optical, electrical and electrochemical properties of Fe: Co 3 O 4 thin films for supercapacitor applications.* Journal of Materials Science: Materials in Electronics, 2017. **28**(24): p. 18951-18965.

75.   Ahmed, A.M., et al., *Enhanced photoelectrochemical water splitting activity of carbon nanotubes@ TiO2 nanoribbons in different electrolytes.* Chemosphere, 2020. **238**: p. 124554.

76.   Jiang, C., et al., *Photoelectrochemical devices for solar water splitting–materials and challenges.* Chemical Society Reviews, 2017. **46**(15): p. 4645-4660.

77.   Choudhary, S., et al., *Nanostructured bilayered thin films in photoelectrochemical water splitting–A review.* International journal of hydrogen energy, 2012. **37**(24): p. 18713-18730.

78.   Fiaz, M., et al., *One pot solvothermal synthesis of Co3O4@ UiO-66 and CuO@ UiO-66 for improved current density towards hydrogen evolution reaction.* Materials Chemistry and Physics, 2020. **239**: p. 122320.

79.   Chang, X., et al., *Enhanced surface reaction kinetics and charge separation of p–n heterojunction Co3O4/BiVO4 photoanodes.* Journal of the American Chemical Society, 2015. **137**(26): p. 8356-8359.

80.   Xu, D., et al., *MOF-derived Co3O4 thin film decorated BiVO4 for enhancement of photoelectrochemical water splitting.* Applied Surface Science, 2019. **491**: p. 497-504.

81.   Chandrasekaran, S., et al., *3D crumpled RGO-Co3O4 photocatalysts for UV-induced hydrogen evolution reaction.* Materials Letters, 2014. **136**: p. 118-121.

82.   Yi, S.S., et al., *Highly efficient photoelectrochemical water splitting: surface modification of cobalt-phosphate-loaded Co3O4/Fe2O3 p–n heterojunction nanorod arrays.* Advanced Functional Materials, 2019. **29**(11): p. 1801902.

83.   Zhao, X., et al., *Three-dimensional plasmonic photoanode of Co3O4 nanosheets coated onto TiO2 nanorod arrays for visible-light-driven water splitting.* International Journal of Hydrogen Energy, 2019. **44**(29): p. 14561-14570.

84.   Dong, G., et al., *Rapid activation of Co 3 O 4 cocatalysts with oxygen vacancies on TiO 2 photoanodes for efficient water splitting.* Journal of Materials Chemistry A, 2018. **6**(42): p. 21003-21009.

85.   Morales-Guio, C.G., L.-A. Stern, and X. Hu, *Nanostructured hydrotreating catalysts for electrochemical hydrogen evolution.* Chemical Society Reviews, 2014. **43**(18): p. 6555-6569.

86.   Mohamed, F., M. Rabia, and M. Shaban, *Synthesis and characterization of biogenic iron oxides of different nanomorphologies from pomegranate peels for efficient solar hydrogen production.* Journal of Materials Research and Technology, 2020. **9**(3): p. 4255-4271.

87.   Shaban, M., et al., *Cyclic voltammetry growth and characterization of Sn–Ag alloys of different nanomorphologies and compositions for efficient hydrogen evolution in alkaline solutions.* RSC advances, 2019. **9**(39): p. 22389-22400.

88.   Kiahosseini, S.R. and H. Ahmadian, *Effect of residual structural strain caused by the addition of Co 3 O 4 nanoparticles on the structural, hardness and magnetic properties of an Al/Co 3 O 4 nanocomposite produced by powder metallurgy.* International Journal of Minerals, Metallurgy and Materials, 2020. **27**(3): p. 384-390.

89.   Al-Aqeeli, N. and I.-u.-H. Toor, *Comparison of Corrosion Behavior of Electrochemically Deposited Nano-Cobalt-Coated Ni Sheet.* Journal of Chemistry, 2013. **2013**: p. 543676.

90.   Lin, C.-Y., et al., *Cobalt sulphide microtube array as cathode in photoelectrochemical water splitting with photoanodes.* Chemical Science, 2014. **5**(12): p. 4906-4913.

91.   Tung, C.-W., et al., *Reversible adapting layer produces robust single-crystal electrocatalyst for oxygen evolution.* Nature communications, 2015. **6**: p. 8106.

92.   Yang, J., et al., *Efficient and sustained photoelectrochemical water oxidation by cobalt oxide/silicon photoanodes with nanotextured interfaces.* Journal of the American Chemical Society, 2014. **136**(17): p. 6191-6194.

93.   Tahira, A., et al., *Advanced Co3O4–CuO nano-composite based electrocatalyst for efficient hydrogen evolution reaction in alkaline media.* International Journal of Hydrogen Energy, 2019. **44**(48): p. 26148-26157.

94.   Wang, J., Q. Zhang, and K. Zhang, *Nonferrous Nanomaterials & Composites for Energy Storage and Conversion*. 2019: Frontiers Media SA.

95.   Cartas, R., et al., *Two analyte calibrations from the transient response of a single potentiometric sensor employed with the SIA technique.* Talanta, 2010. **80**(3): p. 1428-1435.

96.   Tian, H., et al., *Hierarchical (0 0 1) facet anatase/rutile TiO2 heterojunction photoanode with enhanced photoelectrocatalytic performance.* Electrochimica Acta, 2013. **96**: p. 199-205.

97.   Rabia, M., et al., *TiO 2/TiO x N Y hollow mushrooms-like nanocomposite photoanode for hydrogen electrogeneration.* Journal of Porous Materials, 2019: p. 1-7.

98.   Sharma, S., D. Kumar, and N. Khare, *Plasmonic Ag nanoparticles decorated Bi2S3 nanorods and nanoflowers: their comparative assessment for photoelectrochemical water splitting.* International Journal of Hydrogen Energy, 2019. **44**(7): p. 3538-3552.